EFFECT OF ANISOTROPIC NEUTRINO RADIATION ON SUPERNOVA EXPLOSION ENERGY

TETSUYA M. SHIMIZU AND TOSHIKAZU EBISUZAKI

Computational Science Laboratory, The Institute of Physical and Chemical Research (RIKEN), Hirosawa, Wako, Saitama 351-01, Japan;
shimizu@atlas.riken.go.jp

AND

KATSUHIKO SATO[1] AND SHOICHI YAMADA[1]

Department of Physics, School of Science, University of Tokyo, Hongo, Bunkyo, Tokyo 113, Japan

Received 2000 May 11; accepted 2001 January 9

ABSTRACT

Since SN 1987A, many observations have indicated that supernova explosions are not spherical. The cause of the asymmetric explosion is still controversial (e.g., asymmetry in the envelope, the convective engine in the central core or in the proto–neutron star). In our previous study, anisotropic neutrino radiation has been proposed as an explanation for this asymmetry. In this paper we carried out a series of systematic multidimensional numerical simulations in order to investigate the effect of anisotropic neutrino radiation itself on the supernova explosion energy. The neutrino luminosity and the degree of anisotropy in neutrino radiation were assumed as input parameters, and the numerical results for various parameters were compared with each other. It was found that only a few percent of anisotropy in the neutrino emission distribution is sufficient to increase the explosion energy by a large factor. The explosion energy calculated so far in many supernova models has tended to be too short to explain the observation. Anisotropy of 10% in neutrino radiation roughly corresponds to an enhancement of 4% in total neutrino luminosity as far as the explosion energy is concerned. The increase in the explosion energy due to anisotropic neutrino radiation can be explained as follows. Anisotropically emitted neutrinos locally heat the supernova matter and revive a stalled shock wave in the direction of enhanced radiation. The expansion of the gas by the shock propagation results in a decrease in the neutrino cooling (emission) rate that rapidly decreases with the matter temperature. It is this suppression of energy loss that contributes largely to the increase in explosion energy. The efficiency of neutrino heating (absorption) itself is almost unchanged between anisotropic and spherical models with available energy fixed for neutrinos. In order for a stalled shock wave to revive, enhancement of the local intensity in the neutrino flux is of great importance, rather than that of the total neutrino luminosity over all the solid angle. It is first pointed out that such local neutrino heating is capable of triggering a supernova explosion. Anisotropic neutrino radiation is considered to be a plausible mechanism for a "successful" explosion other than the so far suggested "convective trigger."

Subject headings: convection — elementary particles — hydrodynamics — supernovae: general

1. INTRODUCTION

Since SN 1987A is the nearest supernova that has been observed by modern scientific instruments, the explosion energy of collapse-driven supernovae has been best estimated among others. The values for the mass of the envelope, $M_{env} = 6.7\ M_\odot$, and the explosion energy, $E = 1.0 \times 10^{51}$ ergs, have been obtained from an analysis of the light curve (the effect of mixing is also taken into account; Shigeyama, Nomoto, & Hashimoto 1988). On the other hand, Bethe & Pizzochero (1990) have estimated the observed explosion energy of SN 1987A as $1.5 \pm 0.5 \times 10^{51}$ ergs. The discrepancy between these two figures is believed to be due to the degree of matter mixing that they assumed; Shigeyama et al. (1988) assumed whole mixing (see Bethe 1990 for details). In many one-dimensional simulations, the calculated explosion energy is too small unless the effect of convection is included (e.g., Wilson & Mayle 1988, 1993), although Bruenn, Mezzacappa, & Dineva (1995) concluded that the observed value was never reproduced even with convection.

There have been convincing observations that the expanding envelope of SN 1987A was asymmetric (spectropolarimetry, Cropper et al. 1988; speckle interferometry, Papaliolios et al. 1989). It is amazing that the same kind of asymmetry was also observed in SN 1993J by spectropolarimetry (Trammell, Hines, & Wheeler 1993). Hence, it has become more probable that the deformed exploding envelope is a general feature of collapse-driven supernovae. Moreover, many other asymmetric Type II supernovae have been reported by Wang et al. (2001) in polarimetric observations. In particular, the observation of Type Ic SN 1997X (the degree of polarization ∼5%) implies that we may be seeing an asymmetric explosion itself because the core is naked. These observations show that the theoretical models that assume spherical symmetry must be revised.

At present, two-dimensional axisymmetric simulations including the effects of convective instability and neutrino heating, using up-to-date numerical techniques, are the current issue in the context of the explosion mechanism. With Herant, Benz, & Colgate (1992) as the first case, several research groups have carried out multidimensional simulations of supernova cores and extensively discussed the explosion mechanism (Miller, Wilson, & Mayle 1993; Herant et al. 1994; Burrows, Hayes, & Fryxell 1995; Janka & Müller 1996 and references therein and in this paper's list).

Herant et al. (1994) have calculated the supernova core from onset of the collapse, by employing the two-dimensional axial symmetry smoothed particle hydrodynamics (SPH) code. Neutrino transfer and gravitation were included in the framework of spherical symmetry. They succeeded in producing an explosion energy of $\sim 1.2 \times 10^{51}$ ergs. However, their calculations cannot explain the neutron star mass and the Ni production; 1.4 $M_{\odot}$ for the baryon mass of a neutron star (corresponding to a gravitational mass of 1.3 $M_{\odot}$) is somewhat smaller, and ~ 0.6 $M_{\odot}$ Ni is overproduced compared with 0.07 $M_{\odot}$ Ni that has been observed for SN 1987A and SN 1993J. They argued that neutrino heating (hot bubble) convection was enough to explain the explosion energy and that enhancement of the neutrino luminosity was not always necessary. They emphasized the importance of the supply of low-entropy matter, which prevented neutrino heating from decreasing its efficiency. They also argued that the neutrino heating convection is a "robust and self-regulated" mechanism, i.e., the shock wave remains at the same position until it gains enough energy due to convection and, once it gains, the shock stops interacting with a heat reservoir and moves upward. Their SPH code seems to be a little noisy since hydrodynamic quantities are represented by Lagrangian particles that are not distributed in complete spherical symmetry during their infalls. In fact, $\sim 10\%$ of velocity fluctuation even at the collapse stage can be seen in a radial velocity figure of their SPH simulation. Since the amount of the initial fluctuation is very important to the growth time of convective instability, such a large noise could result in overestimating the effect of convection. It is necessary to carry out accurate numerical simulations for convection. Eulerian hydrodynamic simulations are more suitable for this purpose.

Janka & Müller (1994) have numerically calculated the neutrino heating convection with two-dimensional (and three-dimensional) code. They used a Godunov-type scheme called piecewise parabolic method (PPM). Neutrino heating was included with the "light bulb" approximation, where the radiation fields of neutrinos are given by hand, and neutrino heating and cooling rates are estimated and put in the hydrodynamic equations. They have shown that the explosion energy is increased by convective effects, compared with the results of spherical symmetric calculations. However, they concluded that neutrino luminosity enhancement was more important and crucial to explain the explosion energy, based on their extensive parameter research. Janka & Müller (1995, 1996) have shown that the effect of convection is only important if the neutrino luminosity is small and that convection is not always necessary to explain the explosion energy if the neutrino luminosity is sufficiently enhanced.

Burrows & Fryxell (1993) investigated convective effects by using a two-dimensional numerical code in which neutrino transfer is suppressed in the θ-direction of spherical coordinates but calculated independently for each r-direction. They showed that convection develops in a very early phase ("prompt convection") and considered that neutrino luminosity enhancement would lead to an explosion in a shorter timescale than that of the delayed explosion model. Burrows, Hayes, & Fryxell (1995) showed that multidimensional effects are important for a "successful" explosion. They discussed that multidimensional effects facilitate the condition for a shock revival, since the accret-

ed matter gains more entropy during its "cycling" in the convective region and, as a result, the thermal pressure behind the shock front is larger than that by a one-dimensional model ("convective trigger"). It is interesting that they showed in their simulations that the neutrino flux at the surface of the proto–neutron star fluctuates with respect to the angle θ in spherical coordinates.

Bruenn & Mezzacappa (1994) and Bruenn et al. (1995) have studied the effects of convection by a relativistic one-dimensional numerical code including the mixing length theory. They concluded that the neutrino luminosity is not affected by convection. According to their results, convection in the interior of a proto–neutron star would cease before neutrino heating becomes large. Although the effects of large-scale convection were not implemented, various types of detailed physics that concern the supernova mechanism have been included in their simulations. Thus, the effects of convection on supernova explosions are still unresolved. (It is noted here that Liebendoerfer et al. 2000 recently showed that a vigorous [10^{51} ergs] supernova explosion was obtained in a general relativistic one-dimensional simulation with Boltzmann neutrino transport included.)

As already described, there remain considerable discrepancies in the results of the simulations and their interpretations among those authors. The first authors argued that convection due to an unstable entropy distribution outside the proto–neutron star is the most important and provides a very efficient mechanism for neutrino heating and that other types of physics are not the determining factor. In contrast, the second authors argued that the effect of convection is only important in a small range of physical parameters and that enhancement of the neutrino luminosity due to convective neutrino transfer, for example, is most important. This is due in part to a difference in the input physics and numerical methods used in the simulations and also to the complexity of the supernova phenomenon itself and many unknown physical parameters.

The importance of anisotropy in neutrino radiation fields has been suggested in order to explain observed asymmetric features in SN 1987A (Shimizu, Yamada, & Sato 1994). The suggested anisotropic neutrino radiation due to rotation of the neutron star is merely one of the explanations. However, as can be seen in the simulations by Burrows et al. (1995), fluctuation of the neutrino flux with angle and time seems to be a common feature of core collapse supernovae, since the proto–neutron star interior is also convectively unstable. Simulating a rotating proto–neutron star interior, Keil, Janka, & Müller (1996) also reported an anisotropy of $\sim 4\%$ in the neutrino flux. So far, other groups simulating the hot bubble convection have only assumed spherical neutrino radiation (otherwise, perturbed radiation field from spherical symmetry) from the hot neutron star (Herant et al. 1994; Burrows et al. 1995; Janka & Müller 1995, 1996). We investigate here the effect of anisotropic neutrino radiation on the dynamics of hot bubbles and the shock front, by using an accurate numerical code.

The purpose of this study is not to demonstrate the simulation as realistically as possible but instead to perform a systematic survey by a series of simulations to clarify the effect of anisotropic neutrino radiation itself on the explosion dynamics. We also aim at comparing the effect of anisotropy in neutrino radiation with that of "convection." The dynamics of the supernova explosion is very compli-

cated; matter is a mixture of electron gas, heavy iron group nuclei, and photons; nuclear matter appears; neutrinos are transferred and interact with matter; hydrodynamical instabilities grow; those ingredients are coupled with each other. These entangled effects are in general inseparable. The only way to separate each effect is to compare carefully the results of models with different physical parameters. Thus, we carried out a series of numerical simulations, changing the input parameters such as anisotropy in neutrino radiation, the energy of neutrinos, initial perturbation in the infalling medium, and so forth, in order to search for the important mechanism involved in the supernova explosion.

The modeling of anisotropic neutrino radiation and the input physics in the numerical simulation are described in § 2. The results of the simulation and the discussion are presented in §§ 3–5. A model of anisotropic neutrino radiation and the numerical techniques used for this study are described in Appendices A and B, respectively. Several movies produced from the present supernova simulation are also available on the World Wide Web[2] in the Animation GIF and other formats.

2. BASIC EQUATIONS AND ASSUMPTIONS FOR SIMULATION

2.1. Hydrodynamic Equations

The numerical simulations are performed in spherical coordinates, (r, θ). With the assumption of axial symmetry, the basic equations can be presented as

$$\frac{\partial \rho}{\partial t} = -\frac{\partial}{\partial (r^3/3)} (r^2 \rho u_r) - \frac{\partial}{\partial (-r \cos \theta)}$$
$$\times [(\sin \theta) \rho u_\theta] , \quad (1)$$

$$\frac{\partial (\rho u_r)}{\partial t} = -\frac{\partial}{\partial (r^3/3)} (r^2 \rho u_r^2) - \frac{\partial p}{\partial r} - \frac{\partial}{\partial (-r \cos \theta)}$$
$$\times [(\sin \theta) \rho u_r u_\theta] + \frac{\rho u_\theta^2}{r} - \rho \frac{GM}{r^2} , \quad (2)$$

$$\frac{\partial (\rho u_\theta)}{\partial t} = -\frac{\partial}{\partial (r^3/3)} (r^2 \rho u_\theta u_r) - \frac{\partial}{\partial (-r \cos \theta)}$$
$$\times [(\sin \theta) \rho u_\theta^2] - \frac{1}{r} \frac{\partial p}{\partial \theta} - \frac{\rho u_\theta u_r}{r} , \quad (3)$$

$$\frac{\partial (\rho E)}{\partial t} = -\frac{\partial}{\partial (r^3/3)} (r^2 \rho H u_r) - \frac{\partial}{\partial (-r \cos \theta)}$$
$$\times [(\sin \theta) \rho H u_\theta] - \rho u_r \frac{GM}{r^2} + \rho \frac{dq}{dt} , \quad (4)$$

where ρ, u, p, G, M, and dq/dt are the density, the velocity field, the pressure, the gravitational constant, the mass of the neutron star, and the energy source term (neutrino heating and cooling), respectively, and E, H are defined by $E = e + u^2/2$, $H = h + u^2/2$, by using the internal energy per unit mass, e, and the specific enthalpy, $h = e + p/\rho$. The first and last equations (eqs. [1] and [4]) denote mass and energy conservation, respectively. The second and third (eqs. [2] and [3]) are the momentum equations. The gravitational pull of the central neutron star is imposed as in equations (2) and (4). A transformation from the ordinary

coordinate variables (r, θ) is performed in order to rewrite the basic equations in a conservative form as follows:

$$\frac{1}{r^2} \frac{\partial}{\partial r} \to \frac{\partial}{\partial (r^3/3)} ,$$

$$\frac{1}{r \sin \theta} \frac{\partial}{\partial \theta} \to \frac{\partial}{\partial (-r \cos \theta)} .$$

These hydrodynamic equations are solved with an extended version of the Roe scheme that is capable of handling general equations of state in spherical coordinates and capable of reproducing stationary strong shock waves by satisfying all the items of "property U" that Roe (1981) required (see Appendix B for details).

The mesh number is 500×60 in (r, θ) directions, which covers from 50 to 10^4 km in radius. The smallest mesh size is 0.25 km, and 240 grid points are placed within 200 km. The computational region includes the convective region above the neutrino sphere, the Fe core, the Si shell, and part of the CO shell, where the kinetic and thermal energy is directly related to the supernova explosion energy. The region inside the proto–neutron star, however, is excluded in the simulation to save computational time.

2.2. Angular Distribution of Neutrino Flux

Neutrino heating and cooling are incorporated as energy source terms in equation (4) since the simulated region is transparent enough for neutrinos (the "light bulb" approximation without neutrino transport). The exchange of momentum between matter and neutrino radiation is not included for the same reason. Accordingly, both the neutrino radiation field and its total neutrino luminosity are fixed in the same way as those in the initial model throughout each simulated model for simplicity.

In this paper we assume the anisotropic neutrino flux density as

$$l_\nu(r, \theta) = \sqrt{[l_z(r)]^2 \cos^2 \theta + [l_x(r)]^2 \sin^2 \theta} , \quad (5)$$

where the neutrino fluxes along and orthogonal to the axis of symmetry are defined as

$$l_z(r) = \frac{7}{16} \frac{\sigma T_\nu^4 a_x^2}{r^2} , \quad (6)$$

$$l_x(r) = \frac{7}{16} \frac{\sigma T_\nu^4 a_x a_z}{r^2} , \quad (7)$$

respectively. Here (r, θ) represents the spherical coordinates, T_ν is the neutrino temperature of assumed blackbody radiation, σ is the Stefan-Boltzmann constant, and a_x, a_z are the measures of length that converge to the radius of the central neutron star in the case of spherical symmetry. Their ratio, $a_x/a_z = l_z/l_x$, determines the degree of anisotropy in the neutrino radiation field. The basic idea of this assumed neutrino flux is described in Appendix A. The plausibility of the anisotropy in neutrino radiation is discussed in §§ 4.5 and 4.6.

The total luminosity is fixed between the anisotropic and spherical models in order that only effects of neutrino anisotropy are taken into account. For this purpose, the scale of length a_x is calculated for a given ratio, a_x/a_z, by setting

$$L_\nu = \int d\Omega r^2 l_\nu(r, \theta) = \frac{7}{16} \sigma T_\nu^4 4\pi R_{NS}^2 \quad (8)$$

and solving equations (A2) and (A7), where $R_{NS} = 50$ km is the radius of the proto–neutron star for the spherical model.

2.3. Initial Conditions

We used the fact that, in the delayed mechanism, the shock is stalled at a radius of a few hundred kilometers and stays for a few hundred milliseconds. It is a good approximation to exploit the stationary hydrodynamic solution as an initial model. The initial solution is exactly consistent with the input physics that are assumed in the time evolution calculations. In order to maintain consistency between the initial model and the hydrodynamic code, we reproduced the stalled shock wave by solving the stationary hydrodynamic equations:

$$4\pi r^2 \rho v = \dot{m} , \qquad (9)$$

$$v\partial_r v + \frac{1}{\rho}\partial_r p = -\frac{GM}{r^2} , \qquad (10)$$

$$v\left[\partial_r e + p\partial_r\left(\frac{1}{\rho}\right)\right] = \frac{dq}{dt} , \qquad (11)$$

as well as the equation of state (EOS) $p = p(\rho, e)$, where dq/dt is the net neutrino heating and cooling rate, M is the mass of the young neutron star, and $\dot{m}$ is the flux of infalling mass (assumed as constant); all other variables represent the ordinary ones in hydrodynamics.

Since we cannot at present include the effect of either general relativity or neutrino transport on a multidimensional numerical code, we have to carry out a calculation of the supernova core by neglecting these effects. Fortunately, such neglect provides a good approximation for calculations on supernova cores above the neutrino sphere, where the density of matter is not very high and it is not opaque for neutrinos. Only a few percent of total emitted neutrinos are absorbed in this region. The supernova explosion energy, however, predominantly originates from the kinetic and thermal energy there. The effect of neutrinos is thus introduced as energy source and sink terms in dq/dt in equation (11). We have assumed the neutrino temperature T_ν to be 5.0 MeV, the radius of the neutrino sphere to be 50 km, and the energy spectrum of neutrinos to be a blackbody distribution. The corresponding neutrino luminosity is $L_{\nu_e} = 8.8 \times 10^{52}$ ergs s^{-1} and the neutrino flux density $l_{\nu_e} = 2.8 \times 10^{-13}$ foe cm^{-2} s^{-1}; these are assumed to remain constant for simplicity. The neutrino heating and cooling rates used in the simulations are described in § 2.4.

As for the EOS, we have included radiation pressure, gas pressure of nuclei and free nucleons, and pressure of degenerate electrons at zero temperature. The dissociation of iron nuclei via alpha particles into free protons and neutrons is calculated by using Saha's equation for the statistical equilibrium. The transition from iron to neutron-rich nuclei is neglected since the interior of the neutron star is excluded in the simulation. When solving for the initial conditions, the internal energy density, e, was assumed to satisfy $p \approx \rho e/3$ if nuclei are completely dissociated into free nucleons, since this assumption facilitates solving the stationary equations (9)–(11). The same EOS is used in the numerical simulations in §§ 2.5 and 3. We further assumed that cold matter mainly consisting of Fe nuclei is infalling above the shock front with a velocity of 80% of the free-fall velocity. The mass accretion rate is also assumed to be constant in time as $\dot{M} = -0.2 \, M_\odot$ s^{-1}. A shock discontinuity is connected by the Rankine-Hugoniot conditions and placed at the radius of 200 km.

Figure 1 shows the initial model used throughout this study. The profiles for density, velocity, temperature, pressure, photon-to-baryon ratio (proportional to entropy), and net neutrino heating and cooling rates with respect to the radius in km are plotted. It is shown in the entropy plot (Fig. 1e) that a negative entropy gradient exists (80–200 km), which is a site of convective instability. It can be notable that such a negative entropy gradient is a natural consequence of a stationary shock front and that convective instability is thus generally produced in the delayed mechanism. This fact is explained as follows: to support the ram pressure of infalling matter at the shock front, the temperature must rise to ~ 1 MeV behind the shock front; this temperature indicates that heating dominates cooling there. At a smaller radius, however, the temperature increases and grows sufficiently high ($\sim T_\nu$) for cooling to dominate around the neutrino sphere, since the cooling rate is a steep function of the temperature ($\propto T^6$). The location thus exists where the heating rate equals the cooling rate. Note that the left-hand side of equation (11) represents an increase in entropy of the infalling matter, that is, the net heating and cooling rate vanishes at the peak of the entropy profile (Burrows & Goshy 1993). Therefore, the entropy gradient must be negative in the region where the net neutrino rate is positive, as can be seen in the plots of the entropy and the neutrino rate (Figs. 1e and 1f).

2.4. Neutrino Heating and Cooling Rates

The following reactions are included as neutrino heating processes:

$$\left.\begin{array}{l} \nu_e + n \rightarrow p + e^- \\ \bar{\nu}_e + p \rightarrow n + e^+ \end{array}\right\} \quad \text{Absorption by free nucleons ,}$$

$$\left.\begin{array}{l} \nu + e^- \rightarrow \nu + e^- \\ \nu + e^+ \rightarrow \nu + e^+ \end{array}\right\} \quad \begin{array}{l} \text{Scattering off electrons} \\ \text{and positrons ,} \end{array}$$

while the neutrino cooling processes are

$$\left.\begin{array}{l} e^- + p \rightarrow n + \nu_e \\ e^+ + n \rightarrow p + \bar{\nu}_e \end{array}\right\} \quad \begin{array}{l} \text{Neutrino emission due to} \\ \text{electron capture} \end{array}$$

Thermal (photo, pair, plasma) neutrino emission process .

The corresponding heating and cooling rates are given as follows:

$$\left(\frac{dq}{dt}\right)_{abs} = 4.8 \times 10^{32} \text{ ergs s}^{-1} \text{ g}^{-1}$$

$$\times \left(\frac{l_{\nu_e}}{\text{foe s}^{-1} \text{ cm}^{-2}}\right) T_\nu^2 (x_p + x_n) , \qquad (12)$$

$$\left(\frac{dq}{dt}\right)_{NES} = 7.3 \times 10^{31} \text{ ergs s}^{-1} \text{ g}^{-1}$$

$$\times \left(\frac{l_{\nu_e}}{\text{foe s}^{-1} \text{ cm}^{-2}}\right) \frac{(T_\nu - T)T}{\tanh(\alpha\eta/2)} , \qquad (13)$$

$$\left(\frac{dq}{dt}\right)_{cap} = -2.0 \times 10^{18} \text{ ergs s}^{-1} \text{ g}^{-1} T^6 (x_p + x_n)$$

$$\times \left\{1 + \frac{[\eta^6/6 + (5\pi^2/6)\eta^4 + (7\pi^4/6)\eta^2]}{236.5}\right\} \qquad (14)$$
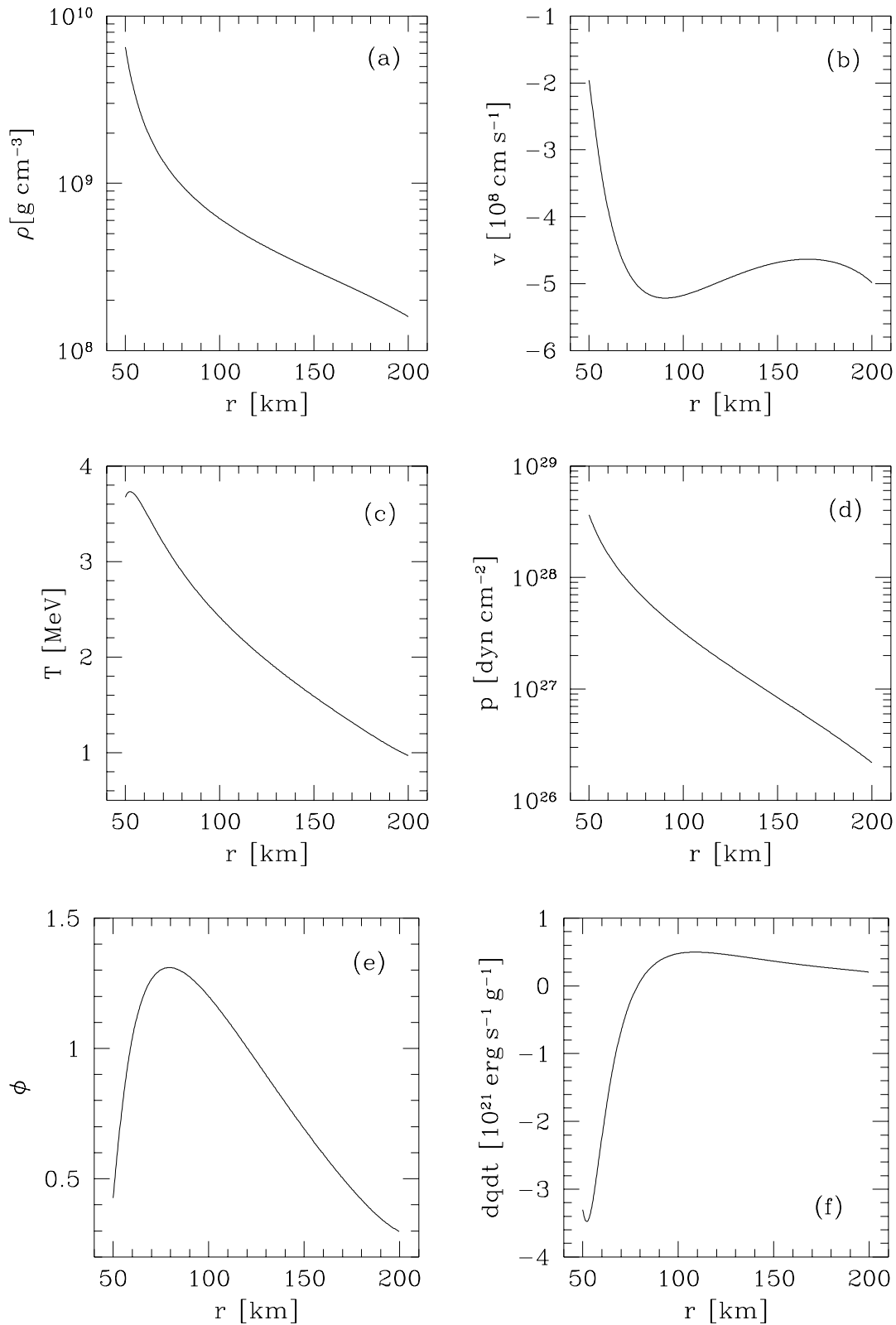
FIG. 1.—Initial model for the simulations; (a) density, (b) velocity, (c) matter temperature, (d) pressure, (e) photon-to-baryon ratio ϕ (~ 0.1 entropy), (f) net neutrino heating and cooling rate dq/dt (heating term minus cooling term); the neutrino sphere and the shock are at 50 and 200 km, respectively.

$$\left(\frac{dq}{dt}\right)_{\text{ppp}} = -1.9 \times 10^{25} \text{ ergs s}^{-1} \text{ g}^{-1} \left(\frac{T^9}{\rho}\right), \quad (15)$$

where the neutrino and matter temperatures, T_ν and T, respectively, are defined in MeV; the density ρ in g cm^{-3},

$\eta = \mu_{e^-}/T$, is the dimensionless chemical potential of electrons; l_{ν_e} is the flux density of electron neutrinos; $(x_p + x_n)$ is the mass fraction of protons and neutrons; $\alpha = (4/3)[\zeta(2)/\zeta(3)] = 1.825$ is a numerical factor; and the unit foe is equivalent to 10^{51} ergs. It is to be noted that the effect of the

chemical potential of electrons has been included in the electron capture term, and the neutrino-electron scattering term is represented by one equation that covers from the electron-degenerate regime to the electron-positron pair dominant regime. The luminosities of electron and anti-electron neutrinos are assumed to be the same and subject to the Fermi-Dirac distribution for simplicity, and the μ and τ neutrinos are not included since their contribution to the heating and cooling rates is not important above the neutrino sphere.

The dimensionless chemical potential, η, in equations (13) and (14) is calculated from the photon-to-baryon (number) ratio,

$$\phi = \frac{n_\gamma}{n_B} = 5.24 \times 10^7 \frac{(T/\text{MeV})^3}{(\rho/\text{g cm}^{-3})} , \tag{16}$$

by using the relation

$$2\zeta(3)Y_e = \phi \mathcal{N}(\eta) , \tag{17}$$

where $\mathcal{N}(\eta)$ is an integral that appears in the formula for the electron number,

$$n_{e^-} - n_{e^+} = 8\pi\left(\frac{kT}{hc}\right)^3 \mathcal{N}(\eta) ,$$

$$\mathcal{N}(\eta) = \int_0^\infty \left(\frac{1}{e^{y-\eta} + 1} - \frac{1}{e^{y+\eta} + 1}\right) y^2 \, dy$$

$$= \frac{1}{3} \eta^3 + \frac{\pi^2}{3} \eta . \tag{18}$$

The photon-to-baryon ratio, ϕ, includes relativistic electrons and positrons and is related to the entropy of the radiation fields per baryon, $s_{\text{rad}} = (4/3)a(kT)^3/n_B$, as

$$s_{\text{rad}} = \frac{11\pi^4}{90\zeta(3)} \phi = 9.904\phi , \tag{19}$$

if the system is electron-positron pair dominant.

The energy deposition is mainly due to the absorption process acting on the shocked matter, so that we can roughly estimate what portion of the energy in the neutrino flux is absorbed as follows:

$$\rho\left[\frac{(dq/dt)_{\text{absorp}}}{l_{v_e}}\right] = (5 \times 10^8 \text{ g cm}^{-3})$$

$$\times (4.8 \times 10^{-19} \text{ cm}^2 \text{ g}^{-1})T_v^2$$

$$= \frac{1.3 \times 10^{-2}}{200 \text{ km}} . \tag{20}$$

Therefore, only a few percent of the neutrino energy is absorbed between the neutrino sphere and the shock front.

The cross sections used for these interactions are presented in Tubbs & Schramm (1975). The cross section for the neutrino absorption by nucleons (eq. [12]) is given by

$$\sigma(v_e n \rightarrow pe^-) \simeq \sigma(v_e p \rightarrow ne^+) \simeq 3.8\sigma_0\left(\frac{E_v}{m_e}\right)^2$$

$$\times \left[\frac{1}{2}\left(\alpha^2 + 1\right) + \frac{1}{4}\left(\alpha^2 - 1\right)\right]$$

$$\simeq (8.6 \times 10^{-44} \text{ cm}^2)E_v^2 , \tag{21}$$

for 1.3 MeV $\ll E_v$ (well satisfied for $T_v = 5$ MeV; $E_v = 3.2T_v$ for the Fermi-Dirac distribution), where $c = 1$, E_v is the

average neutrino energy in MeV, m_e is the electron mass, $\alpha \simeq 1.2$ is the correction due to the nucleon structure, and $\sigma_0 = 4G^2m_e^2\hbar^2/\pi c^2 \simeq 1.7 \times 10^{-44}$ cm^2 is the typical cross section for the weak interaction. The cross sections for neutrino scattering off electrons and positrons (eq. [13]) are

$$\sigma_{e^+ + e^-} = \frac{7}{8}\sigma_0 \frac{E_v T}{(m_e)^2} \quad \text{for } v_e ,$$

$$= \frac{3}{8}\sigma_0 \frac{E_v T}{(m_e)^2} \quad \text{for } \bar{v}_e . \tag{22}$$

An effective factor $(T_v - T)/T$ is introduced into the formula for scattering (eq. [13]) in order to take into account the ratio of translated energy per scattering. The hyperbolic tangent originates from the sum of the electron and positron number density, $n_{e^-} + n_{e^+}$. The formula for the electron capture (eq. [14]) is obtained from Takahashi, El Eid, & Hillebrandt (1978). Note that $(dq/dt)_{\text{abs}} \propto T_v^6$ for neutrino absorption, while $(dq/dt)_{\text{cap}} \propto T^6$ for electron capture. This is because the incident particles contribute to the reaction, they are subject to the Fermi-Dirac distribution, and the cross sections are proportional to the temperature squared. For thermal neutrino emission (eq. [15]), a fitting formula is used, which is a good fit in the ranges of temperature and density involved, $0.86 < T < 8.6$ MeV and $\rho < 10^{10}$ g cm^{-3}, respectively (Itoh et al. 1989).

2.5. Simulated Models

Numerical simulations were carried out in order to investigate the effects of anisotropic neutrino radiation. The neutrino energy and the degree of anisotropy were changed to model various anisotropic explosions. The neutrino flux distribution is presented in § 2.2 (eq. [5]), as well as in Appendix A in detail. All the simulated models in the present study are listed in Table 1 for reference. The most significant physical parameters for the simulations are the ratio of neutrino flux densities between the polar and equatorial directions, l_z/l_x, and the neutrino temperature on the emitting surface, T_v. These parameters were changed in a series of numerical simulations to clarify how important each effect is. The assumed values of these parameters are $l_z/l_x = 1.5, 1.2, 1.05$, and 1.0, $T_v = 5.0, 4.8, 4.7$, and 4.6 MeV, and so on (Table 1). As shown later in § 3, the model for $T_v = 5.0$ MeV corresponds to an energetic-explosion model due to the enhanced neutrino luminosity, while the model for $T_v = 4.6$ MeV is a "failed" weak-explosion model (the explosion energy is insufficient) as far as spherical symmetry is concerned; the spherical 4.7 and 4.8 MeV models are in the transient region. The rather weakly explosive model ($T_v = 4.7$ MeV) serves as a fiducial model in the following sections.

The same EOS as the initial conditions (§ 2.3) is used for consistency. The total neutrino luminosity was fixed constant for each model throughout the simulation for simplicity. We would not like to introduce any complication such as whether the decay time of neutrino luminosity is equal or not between the spherical and anisotropic models. According to one-dimensional simulations by Mayle (1985), the timescale for the decay in luminosity is about 500 ms after bounce for various models of 12, 15, 25, and 50 $M_\odot$. Thus, the simulations were ended (at t_{end} in Table 1) before 500 ms had elapsed after the shock stagnation.

The case of density perturbation only was also calculated and compared with that of the anisotropic neutrino radi-

TABLE 1

SIMULATED MODELS

Model	l_z/l_x	T_ν (MeV)	$\delta\rho/\rho$ (%)	K(AV)	t_{end} (ms)	$E_{exp}^{(80)a}$ (foe)	$E_{exp}^{(200)b}$ (foe)
facg47..........	1.00	4.70	0	1.0	500	0.053	0.065
facg10547......	1.05	4.70	0	1.0	476	0.072	0.276
facg1247	1.20	4.70	0	1.0	474	0.111	0.355
facg46..........	1.00	4.60	0	1.0	500	0.053	0.064
facg1546	1.50	4.60	0	1.0	367	0.079	0.258
frho1047	1.00	4.70	10[c]	1.0	459	0.055	0.256
frho1p47	1.00	4.70	1[c]	1.0	500	0.053	0.065
fr10ff47	1.00	4.70	10[d]	1.0	290	0.106	0.324
fr1pff47	1.00	4.70	1[d]	1.0	246	0.053	0.193
facg10247......	1.02	4.70	0	1.0	94	0.053	...
facg1147	1.10	4.70	0	1.0	82	0.096	...
facg1347	1.30	4.70	0	1.0	80	0.118	...
facg50..........	1.00	5.00	0	1.0	101	0.187	...
facg12..........	1.20	5.00	0	1.0	92	0.231	...
facg15..........	1.50	5.00	0	1.0	87	0.247	...
facg48..........	1.00	4.80	0	1.0	104	0.154	...
facg1248	1.20	4.80	0	1.0	88	0.151	...
facg475	1.00	4.75	0	1.0	105	0.110	...
fk021247.......	1.20	4.70	0	0.2	80	0.111	...
fk051247.......	1.20	4.70	0	0.5	81	0.111	...
fk0212	1.20	5.00	0	0.2	91	0.228	...
fk0512	1.20	5.00	0	0.5	91	0.230	...
fk0215	1.50	5.00	0	0.2	87	0.247	...

[a] Explosion energy at $t = 80$ ms.
[b] Explosion energy at $t = 200$ ms.
[c] Initial perturbation added only behind the shock.
[d] Initial perturbation added all through the infalling matter.

ation. An initial perturbation of 10% or 1% in density (a sinusoidal distribution) was given either to the shocked matter behind the shock wave or to all the infalling matter (see § 4.4 for details). In addition, the strength of the artificial viscosity (coefficient K; see §§ 4.11 and B4) was changed for some models in order to test its influence on the numerical results.

3. RESULTS

It was found that the asymmetric explosion as a consequence of anisotropic neutrino radiation was a common feature for a wide range of explored parameters. Figures 2 and 3 show the resulting entropy distribution for the anisotropic models of $l_z/l_x = 1.2$ (facg12) and 1.5 (facg15), where the neutrino temperature T_ν is 5.0 MeV, while Figures 4 and 5 are for the models of $l_z/l_x = 1.2$ (facg1247) and 1.05 (facg10547), where $T_\nu = 4.7$ MeV. The contour represents the photon-to-baryon ratio, ϕ, or the entropy: it is to be noted here that the entropy is given by 9.904ϕ in the radiation-dominant region such as that existing behind the shock. The shock front is around 1000–1200 km in Figures 2 and 3 (the crowded contour lines there represent the shock discontinuity). The next crowded group of contour lines inside the shock front show the boundary of a high-entropy region produced due to neutrino heating. The peak in entropy was attained on the axis of symmetry at the radius of ~600 km. The entropy decreased to the state of degeneracy as the central neutron star was approached. The hot proto–neutron star is at the origin of the figure with a radius of 50 km. The maximum and minimum values of the photon-to-baryon ratio, ϕ, are displayed at the bottom of each contour map. The scattered arrows represent the

velocity field. The cold degenerate material is freely falling onto the shock front from the outer part of the iron core and the silicon shell. The value for the velocity displayed at the lowermost right corner is typical for the free-falling matter, and the values for other parts can be obtained by comparing the length of the arrow with this typical value. In
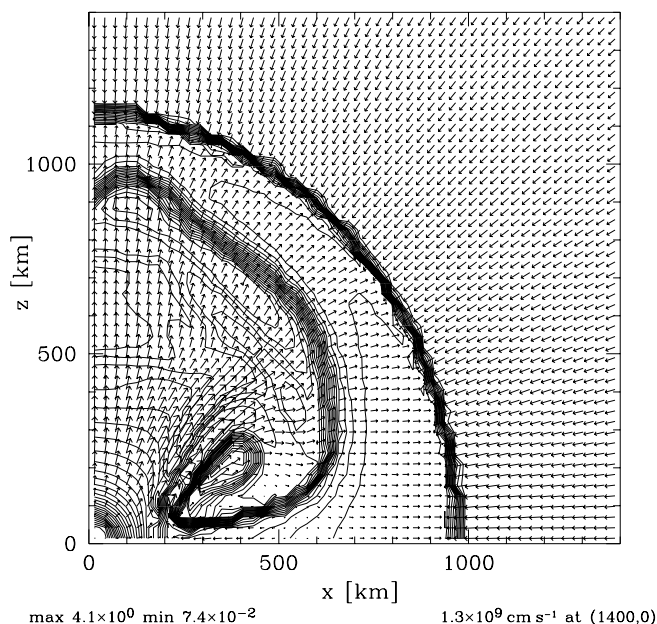

max 4.1×10^0 min 7.4×10^{-2} 1.3×10^9 cm s^{-1} at (1400,0)

FIG. 2.—Contour map of the photon-to-baryon ratio, ϕ, and the velocity field for the model of $l_z/l_x = 1.2$ and $T_\nu = 5.0$ MeV (facg12) at $t = 92$ ms after the shock stall.
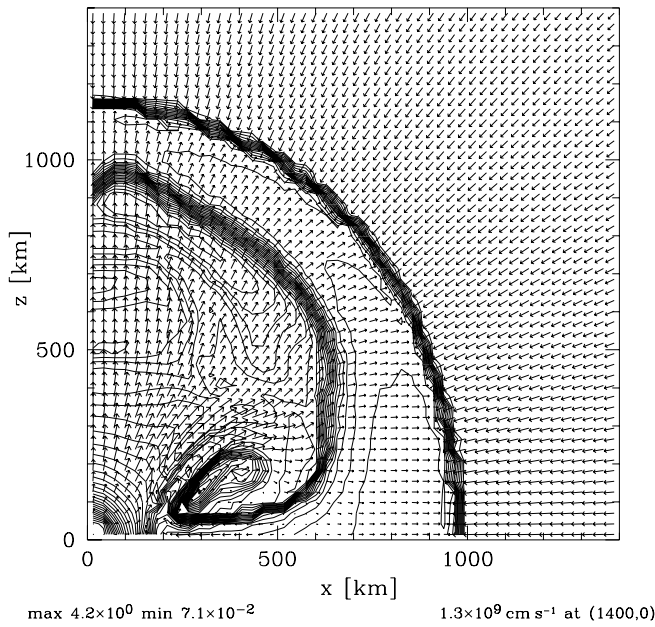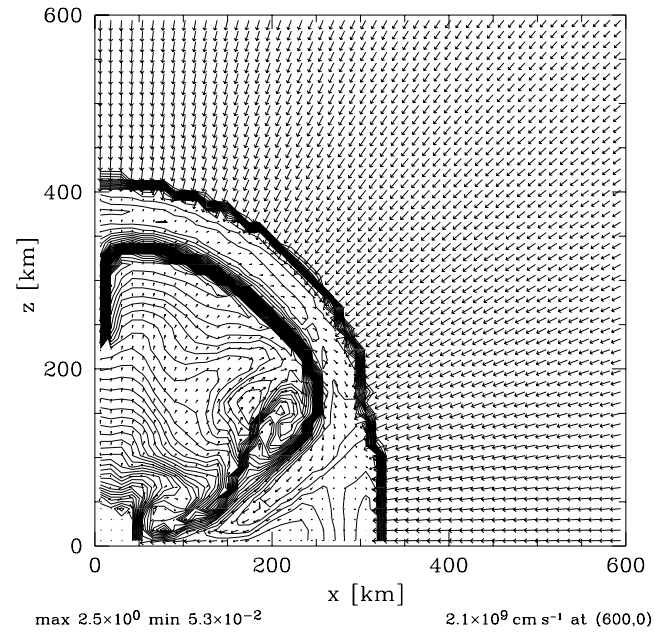
max 4.2×10⁰ min 7.1×10⁻²   1.3×10⁹ cm s⁻¹ at (1400,0)

FIG. 3.—Contour map of the photon-to-baryon ratio, ϕ, and the velocity field for the model of $l_z/l_x = 1.5$ and $T_\nu = 5.0$ MeV (*facg15*) at $t = 87$ ms after the shock stall.

max 2.5×10⁰ min 5.3×10⁻²   2.1×10⁹ cm s⁻¹ at (600,0)

FIG. 5.—Contour map of the photon-to-baryon ratio, ϕ, and the velocity field for the model of $l_z/l_x = 1.05$ and $T_\nu = 4.7$ MeV (*facg10547*) at $t = 84$ ms after the shock stall.

Figures 2, 3, 4, and 5, the high-entropy bubbles are formed around the symmetrical axis, and their upward velocity fields can be clearly seen in those figures. The jetlike explosion is a general feature for anisotropically radiating models. This is also the case even if the neutrino temperature is high. We also calculated some models in which the total neutrino luminosity (L_ν) or the neutrino temperature (T_ν) is changed. (It is to be noted that there is great ambiguity in the total neutrino luminosity estimated by many simulations at present. It will differ depending on the

treatment of neutrino transport, that of interaction between neutrinos and materials, and the adopted properties of the high-density nuclear matter and heavy nuclei.) The case of large neutrino luminosity is represented by the models where $T_\nu = 5.0$ MeV is assumed (Fig. 2, *facg12*) for the same degree of anisotropy as a less luminous model (Fig. 4, *facg1247*). The difference in the shock position of model *facg12* from model *facg1247* is owing to the increased pressure behind the shock front due to the large neutrino heating rate. By comparing Figures 2 (*facg12*) and 3 (*facg15*), it is clearly seen that the resulting asymmetry in the explosion is saturated if the anisotropy in neutrino radiation is as high as $l_z/l_x = 1.2$ (*facg12*).

Considerable mass accretion can be seen around the equatorial plane in Figures 4 and 5. This accretion is due to the low neutrino flux along the equatorial plane. The lower pressure on the equatorial plane due to the smaller neutrino heating allows mass accretion even if the shock wave is moving forward. A strong explosion and heavy accretion take place at the same time. This is one of the distinctive features of the models with anisotropic neutrino radiation. This accretion was also found in the models for $T_\nu = 5.0$ MeV (Figs. 2 and 3), even if the explosion is energetically driven by a large neutrino luminosity.

Time-sequence color-scale maps of the entropy are displayed in Figures 6, 7, 8, and 9. In each figure, the color-scale bar is plotted at the bottom. The red and blue colors represent high and low entropies, respectively. The color boundary between dark blue and light blue shows the shock front. The red region indicates that intense neutrino heating takes place there and the matter entropy becomes high. Time is indicated in each panel, elapsing from the bottom left panel to the bottom right and then from the top left to the top right. The early-time growth of the high-entropy bubble is displayed in Figure 6 for the model of $l_z/l_x = 1.2$ and $T_\nu = 4.7$ MeV (*facg1247*). The matter surrounding the neutron star is first heated along the pole, and a high-
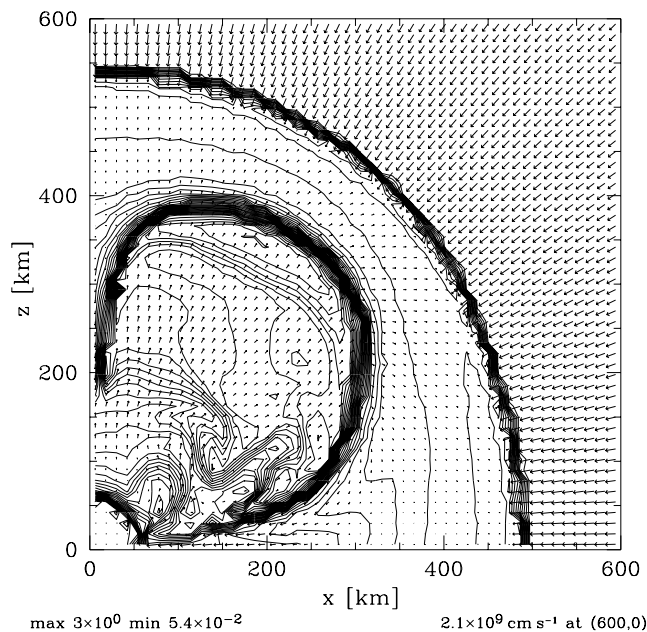

max 3×10⁰ min 5.4×10⁻²   2.1×10⁹ cm s⁻¹ at (600,0)

FIG. 4.—Contour map of the photon-to-baryon ratio, ϕ, and the velocity field for the model of $l_z/l_x = 1.2$ and $T_\nu = 4.7$ MeV (*facg1247*) at $t = 82$ ms after the shock stall.
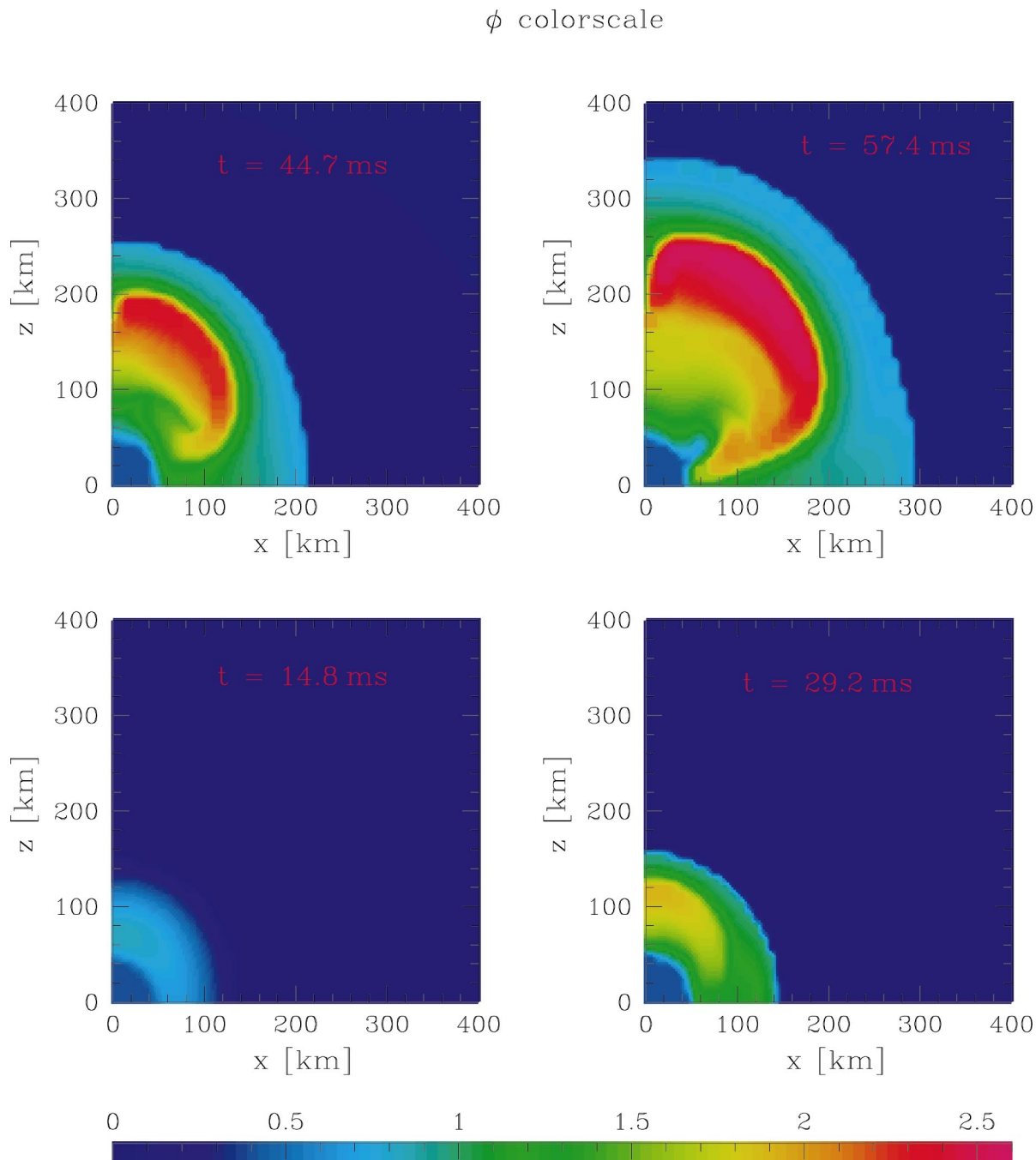
ϕ colorscale

FIG. 6.—Plots of the entropy distribution (ϕ) in time sequence for the model of $l_z/l_x = 1.2$ and $T_\nu = 4.7$ MeV (*facg1247*) during the relatively early stages. The growth of a high-entropy hot bubble is clearly seen.

entropy region is formed there. Since there is a gravitational pull by the central neutron star, the high-entropy bubble moves upward as a result of buoyancy. The high pressure of the heated matter then pushes up the shock front, which deviates from spherical symmetry. The distortion of the shock wave continues and is not diminished in the course of the shock propagation as shown in Figure 7 (slightly later stages than those in Fig. 6). The essential behavior is the same for the case of less anisotropy, $l_z/l_x = 1.05$ and $T_\nu = 4.7$ MeV (*facg10547*), as that in Figure 8, although the revival of the shock wave is somewhat retarded. As shown in Figure 9, the growth of the jetlike motion of the high-entropy bubble becomes prominent in relatively late stages of the explosion for the model of $l_z/l_x = 1.05$ and $T_\nu = 4.7$

MeV (*facg10547*). The large mushroom-like structure of the hot bubble is produced as a result of the global circular motion behind the shock front. The circulation is clockwise in these figures: the matter is moving upward in the high-entropy region and downward in the cool accreted material with respect to the comoving frame of the shock front. The cycle is only a few rotations per explosion. In this sense, the frequently used term "convection" among supernova researchers seems to be inappropriate for the hydrodynamic instability that exists outside the neutron star.

Several degrees of anisotropy in the neutrino radiation were also investigated and compared with each other. In Figure 10, entropy color-scale maps of four models with different anisotropies are plotted. The top left panel is for an
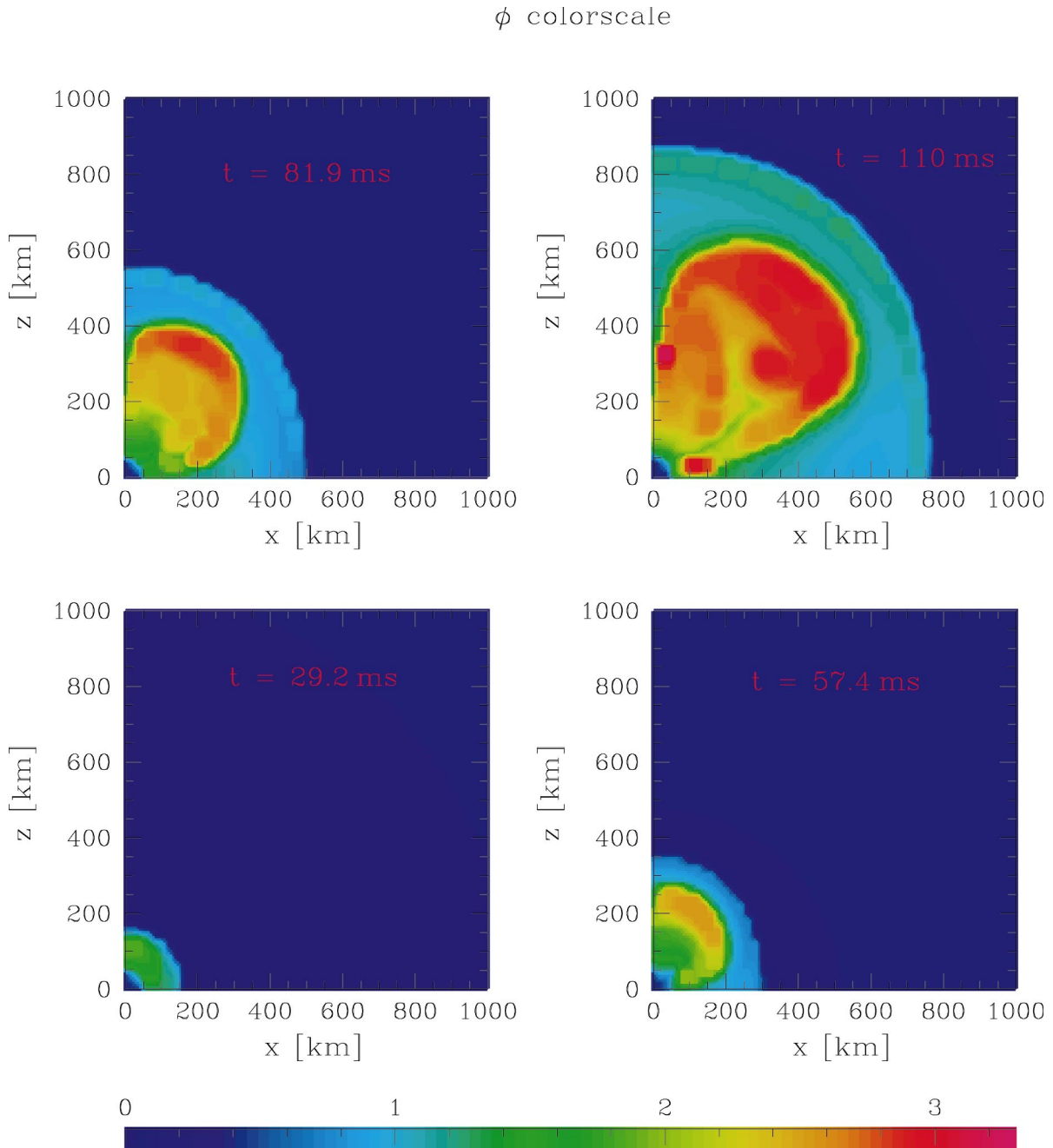
ϕ colorscale

FIG. 7.—Same as Fig. 6 (*facg1247*), except at the slightly later stages. The shock front is distorted as a result of the jetlike motion of the high-entropy bubble.

anisotropic model ($l_z/l_x = 1.2$, *facg1247* at $t = 82$ ms), the top right is for another less anisotropic model ($l_z/l_x = 1.05$, *facg10547* at $t = 84$ ms), the bottom left is for a nearly spherical model ($l_z/l_x = 1.02$, *facg10247* at $t = 94$ ms), and the bottom right is for a spherical model ($l_z/l_x = 1.0$, *facg47* at $t = 98$ ms). The neutrino temperature is identical for all the models here ($T_\nu = 4.7$ MeV). The color-scale bars are different between the four figures and are displayed in each panel on the right end. Figure 10 shows that the effect of anisotropic neutrino radiation strongly depends on the degree of anisotropy. The small-degree anisotropic model of $l_z/l_x = 1.02$ (*facg10247*) is similar to the spherical model (*facg47*). However, an anisotropy of $l_z/l_x = 1.05$ (*facg10547*) is enough for the stalled shock to revive early and results in an asymmetric explosion. The energy evolution is also

much different from the spherical case as discussed later. The larger anisotropy in the neutrino fields is input, and the larger asymmetry in the explosion is obtained, although the asymmetry in the explosion seems to be saturated around the models of $l_z/l_x = 1.2$ (*facg1247*) and 1.3 (*facg1347*). Furthermore, the high-entropy region grows faster for the more anisotropic models. The maximum value is ~ 30 for the anisotropic model of $l_z/l_x = 1.2$ (*facg1247*), while it is ~ 15 for the spherical model of $l_z/l_x = 1.0$ (*facg1247*). The difference between the anisotropic and spherical models is more and more prominent at the later stage of the explosion. The shock position, the profile of the shock front, the evolution of the high-entropy bubble, and the jetlike motion are all considerably different between these models, although the total luminosity is fixed to the same value. Figures 11 and
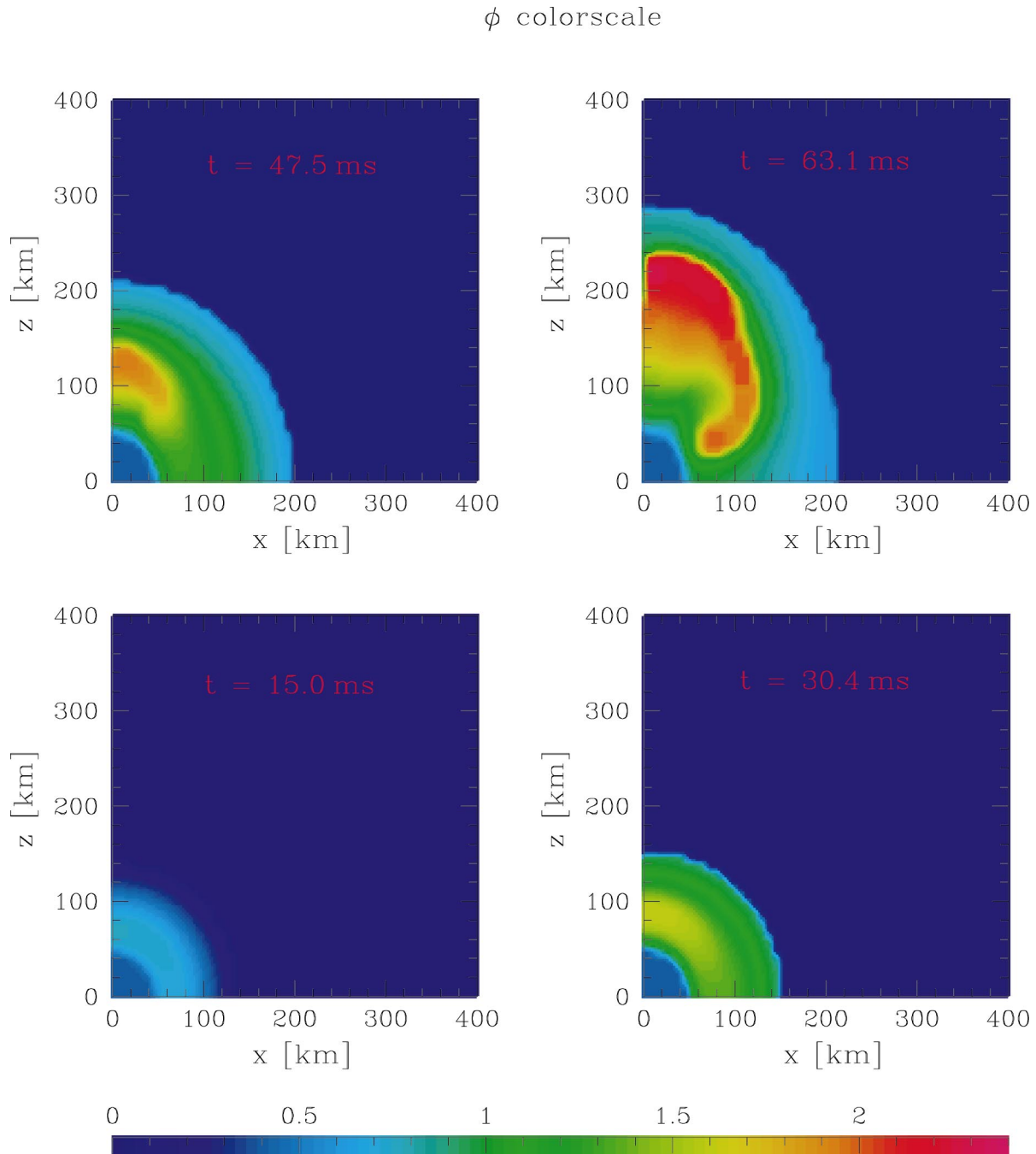
ϕ colorscale

FIG. 8.—Plots of the entropy distribution in time sequence for the model of $l_z/l_x = 1.05$ and $T_\nu = 4.7$ MeV (*facg10547*) during the relatively early stages. The growth of the hot bubble is essentially the same as that of *facg1247* (Fig. 6), except for slow evolution in this less anisotropic case.

12 are for comparison between the anisotropic and spherical models. These figures show the entropy contour and velocity field at almost the same time after the beginning of the simulation, although the axis scales are much different between them. The position of the shock front is much different, and accordingly, the maximum value of entropy for the anisotropic model (~ 40 for *facg10547*) is larger than that for the spherical model (~ 35 for *facg47*).

The effect of the anisotropic neutrino radiation on the explosion energy was then investigated in detail. The explosion energy is defined here as the summation of the total (thermal, kinetic, and gravitational) energy over the region where the total energy is positive. The explosion energies $E_{exp}^{(80)}$ and $E_{exp}^{(200)}$ at 80 and 200 ms, respectively, after the

shock stalls are listed in Table 1 for comparison. Figure 13 shows the time evolutions of the explosion energy, as well as the thermal, kinetic, and gravitational energies, for each model of $T_\nu = 4.7$ MeV. Although even the spherical model (*facg47*) finally explodes, the rate of energy gain for the anisotropic models (*facg1247* and *facg10547*) is considerably larger [see also the corresponding $E_{exp}^{(200)}$ in Table 1]. The anisotropy in neutrino radiation is capable of triggering the explosion and even determines the final value of the explosion energy. Figure 14 shows a comparison of the typical anisotropic model (*facg1247*, $T_\nu = 4.70$ MeV) with different neutrino temperature models, where $T_\nu = 4.70$, 4.75, and 4.80 MeV (spherical *facg47*, *facg475*, *facg48*). As shown in Figure 14 and Table 1 [see the corresponding
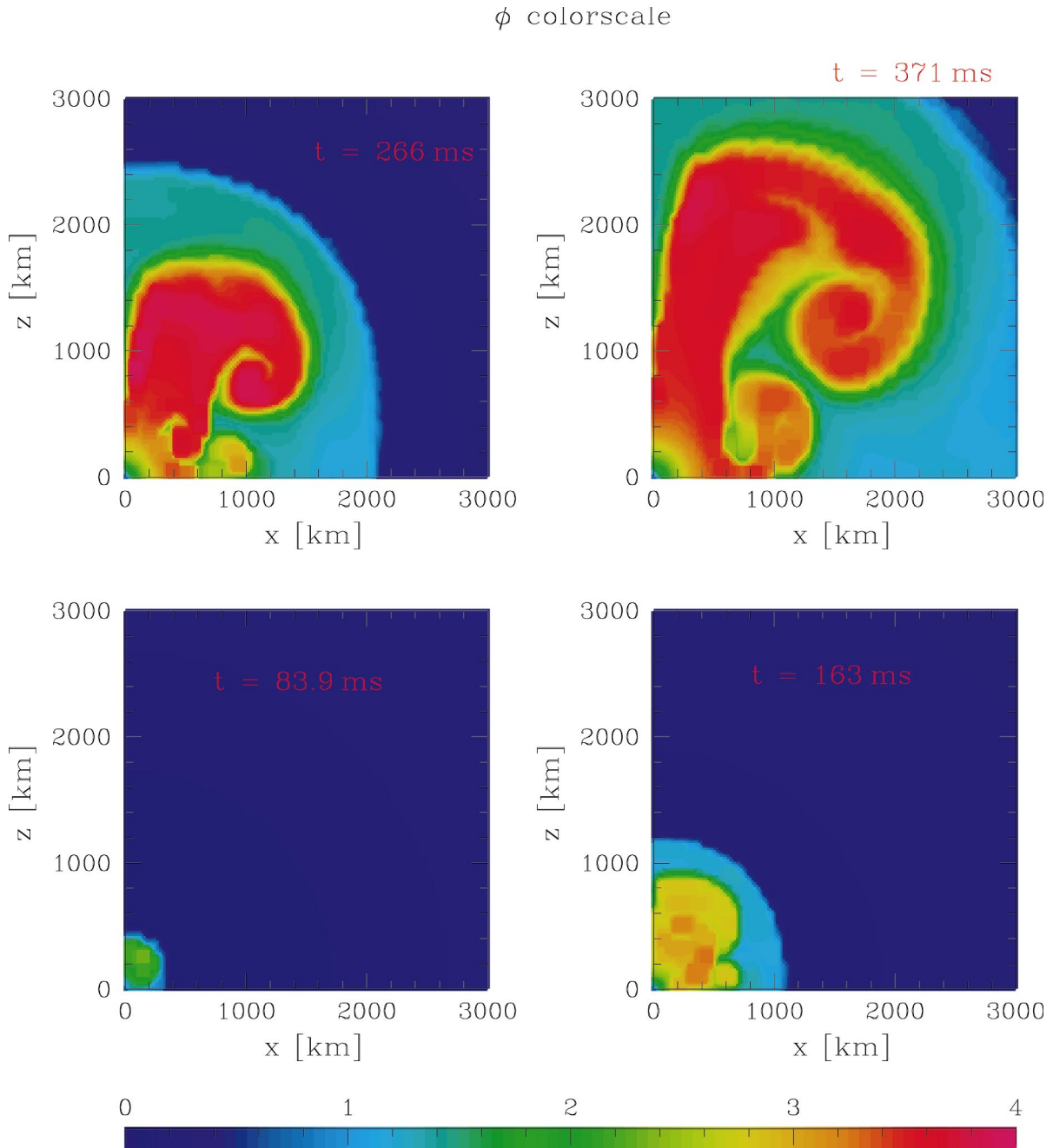
FIG. 9.—Same as Fig. 8 (*facg10547*), except at the late stages. Note the jetlike motion in the high-entropy hot bubble.

$E_{exp}^{(80)}$], it was found that the explosion energy evolution was very similar between models *facg1247* and *facg475*. Therefore, an anisotropy of 10% in neutrino radiation (note that the amplitude of anisotropy is 10% for the model of $l_z/l_x = 1.2$, which is the ratio between the maximum and minimum values) roughly corresponds to an enhancement of $\sim 4\%$ ($= [(4.75 \text{ MeV})^4 - (4.70 \text{ MeV})^4]/(4.70 \text{ MeV})^4$) in total neutrino luminosity, with respect to the effect on the explosion energy. In other words, a shortage of 4% in the neutrino luminosity is supplemented with an anisotropic neutrino radiation of 10%.

As for models with less neutrino luminosity ($T_\nu = 4.6$ MeV), two cases were simulated in which $l_z/l_x = 1.5$ (*facg1546*) and 1.0 (spherical *facg46*). Qualitatively same results for the asymmetric properties as those of the more

luminous model ($T_\nu = 4.7$ MeV) were obtained, although the shock wave was weaker and more slowly moving outward. The difference in asymmetry between the anisotropic and spherical models, however, becomes much more pronounced as the total neutrino luminosity decreased. Figure 15 shows the energy evolution for the very weakly luminous models ($T_\nu = 4.6$ MeV). The explosion energy for the anisotropic model was higher than that of the spherical model as shown in Figure 15 and Table 1 [$E_{exp}^{(200)}$ for *facg46* and *facg1546*], like the case of the more luminous models. Spherical model *facg46* failed to explode, while the anisotropic model *facg1546* was able to explode energetically. The effect of anisotropic neutrino radiation becomes increasingly more important as the total neutrino luminosity decreased. In the case of the total luminosity being
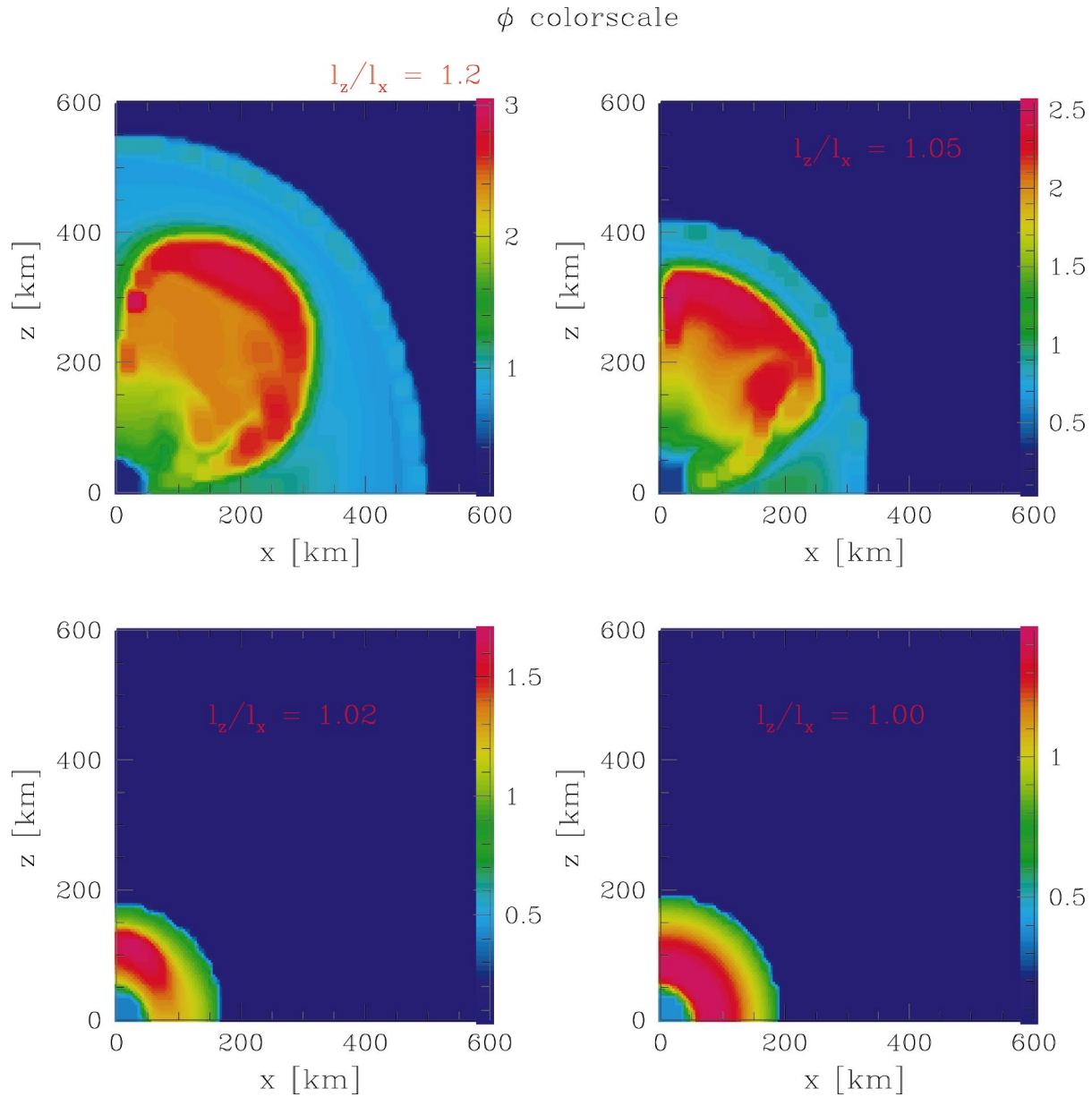
ϕ colorscale

FIG. 10.—Color-scale maps of the photon-to-baryon ratio, ϕ, for models of $T_v = 4.7$ MeV; the corresponding parameters are $l_z/l_x = 1.2$ (*facg1247* at $t = 82$ ms), 1.05 (*facg10547* at $t = 84$ ms), 1.02 (*facg10247* at $t = 94$ ms), and 1.0 (spherical model, *facg47* at $t = 98$ ms), respectively, from top left to bottom right. Time is counted from the shock stall. Note that the color bars are different, which indicates a rapid increase in entropy for the anisotropic models. Anisotropy of $l_z/l_x \sim 1.05$ is necessary for an asymmetric explosion.

marginally insufficient, the anisotropy in neutrino emission becomes a crucial point for an explosion. On the other hand, when a large neutrino temperature is assumed, like $T_v = 5.0$ MeV, the difference in the energy gain rate between the anisotropic and spherical models is significantly diminished [see $E_{exp}^{(80)}$ for *facg50*, *facg12*, and *facg15* in Table 1]. If the total neutrino luminosity is sufficiently enhanced like that, the effect of multidimensions is less important and the energetic explosion is attained only because of the high luminosity of neutrinos. This tendency was also concluded in the simulation survey by Janka & Müller (1995, 1996).

The explosion energy was increased as a result of anisotropic neutrino radiation like that shown in Figures 13–15. The reason for this is considered to be as follows. Neutrino heating rate was found to be almost the same between the anisotropic and spherical models, since its effect was domi-

nated by the neutrino temperature and hence the luminosity. Rather than that, the heating rate was even larger for the spherical model because of the concentration of matter at the center. It is the suppression of neutrino cooling, however, that contributes to the energy gain and thus the explosion energy. This is clearly shown in Figure 16 where the accumulation of the absorbed and emitted energies due to neutrino heating and cooling (only the region outside the neutrino-emitting surface is taken into account) is plotted for both anisotropic (*facg1247*) and spherical (*facg47*) models. The behavior of the neutrino cooling is merely a result of the revival of the shock wave and the decrease in temperature behind the shock. Notice here the decrease in the neutrino emission rate for the anisotropic model (*facg1247*) at around 80 ms in Figure 16 and compare it with the shock positions in Figure 7 at $t = 81.9$ ms. Around
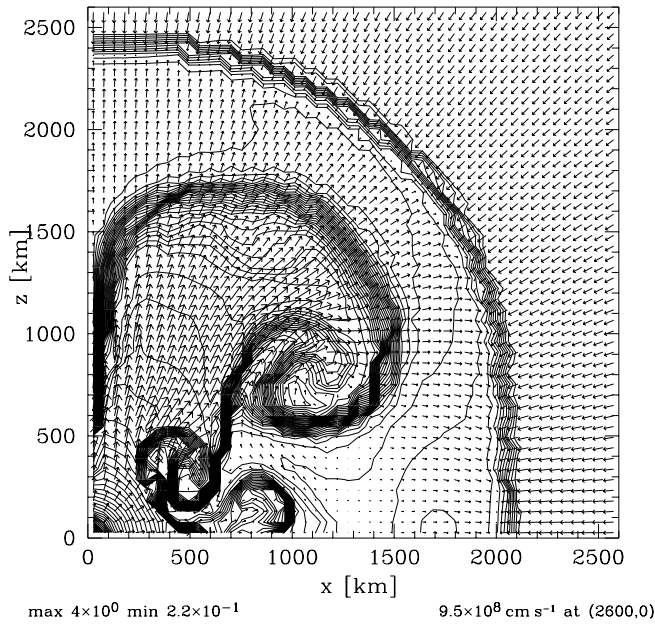
FIG. 11.—Contour map of the photon-to-baryon ratio, ϕ, and the velocity field for the model of $l_z/l_x = 1.05$ and $T_v = 4.7$ MeV (*facg10547*) at $t = 266$ ms after the shock stall. The same model as the top left panel of Fig. 9.

FIG. 13.—Time evolution of the kinetic and thermal, explosion, and gravitational energies for various models with the neutrino temperature $T_v = 4.7$ MeV. *Solid line*: $l_z/l_x = 1.2$ (*facg1247*); *long-dashed line*: 1.05 (*facg10547*); *short-dashed line*: 1.0 (spherical model, *facg47*).

this time, in fact, the shock wave is already launched. The revival of the shock is only resulting from locally intense neutrino heating due to the anisotropic neutrino radiation. An increase in globally averaged thermal energy due to neutrino heating or cooling is not always necessary. Under the anisotropic neutrino radiation field, matter is locally heated only along the axis of symmetry. The thermal pressure around the heated matter is high, and hence it pushes part of the shock wave outward. It should be noted here
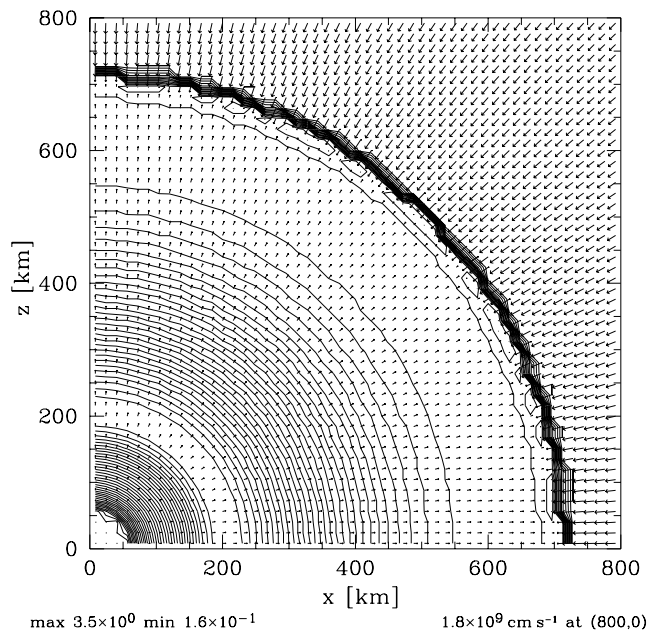
that the Rankine-Hugoniot condition is merely a local relation between both sides of the shock so that a shock revival in one direction is enough; the other part of the shock will follow since the pressure gradient does work along the shock front. The progress of the shock then decreases the temperature as well as the density of the matter behind the shock front. The decrease in the temperature suppresses the neutrino emission due to the electron capture, since the

FIG. 12.—Contour map of the photon-to-baryon ratio, ϕ, and the velocity field for the model of $l_z/l_x = 1.0$ (spherical) and $T_v = 4.7$ MeV (*facg47*) at $t = 271$ ms after the shock stall. Compare with Fig. 11 to see the difference in the maximum entropy value and the shock position.
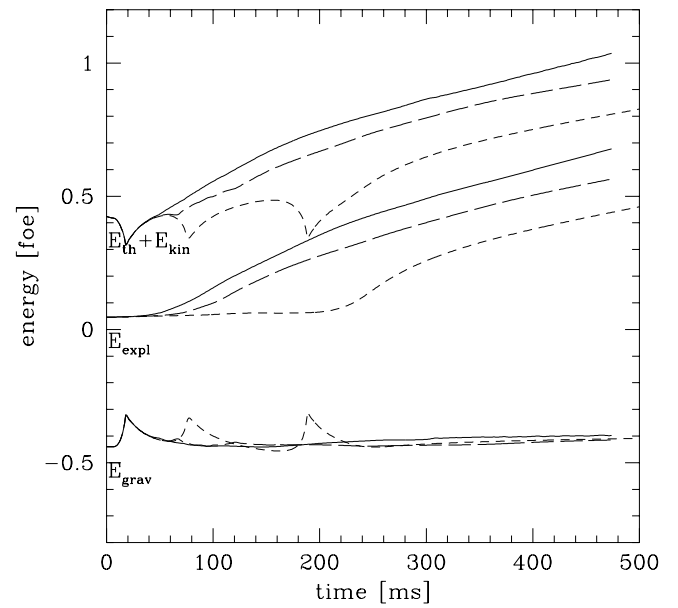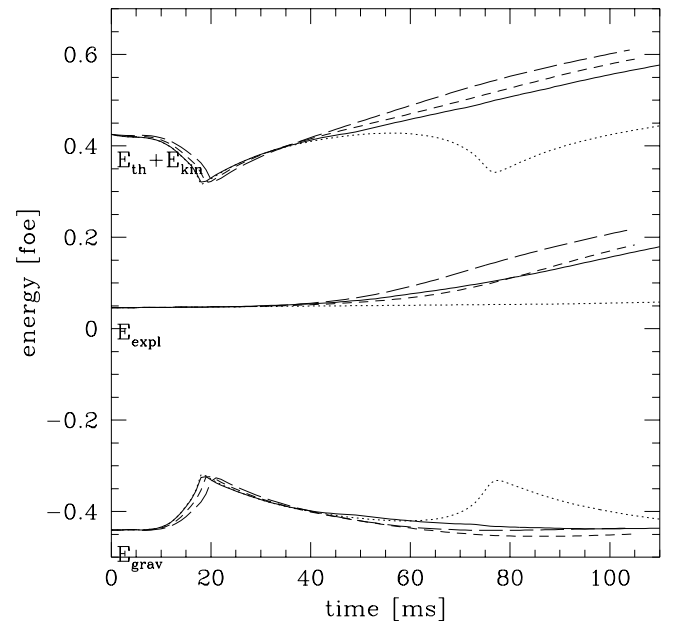

FIG. 14.—Time evolution of the energies for various models in the first 100 ms. *Solid line*: $l_z/l_x = 1.2$ and $T_v = 4.70$ MeV (anisotropic *facg1247*); *short-dashed line*: $T_v = 4.75$ MeV (spherical *facg475*); *dotted line*: $T_v = 4.70$ MeV (spherical *facg47*); *long-dashed line*: $T_v = 4.80$ MeV (spherical *facg48*). The explosion energy for *facg1247* is similar to that for *facg475*.
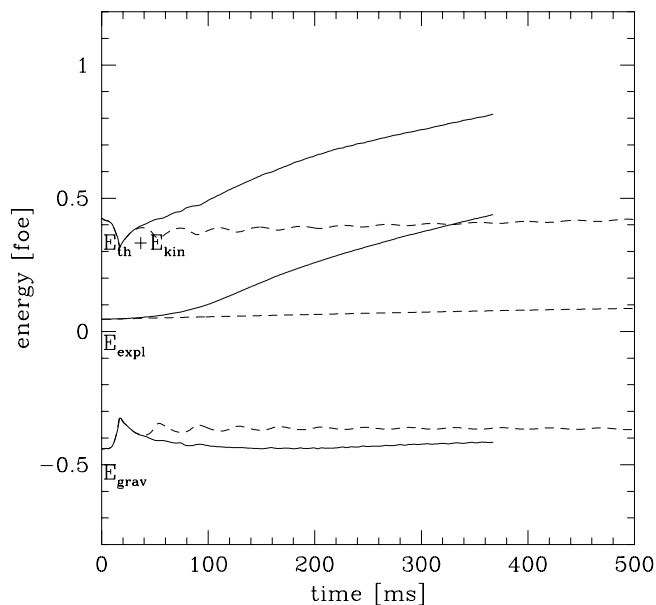
FIG. 15.—Time evolution of the energies for various models with the neutrino temperature $T_v = 4.6$ MeV. *Solid line:* $l_z/l_x = 1.5$ (*facg1546*); *dashed line:* 1.0 (spherical *facg46*).

emission rate is a very sensitive function of the matter temperature, roughly proportional to T^6. Finally, the explosion energy increases because of the suppression of neutrino cooling.

4. DISCUSSION

4.1. Mechanism for the Increase in Explosion Energy

The anisotropy in neutrino radiation was found to be capable of boosting the explosion energy of a supernova. The reason for this is not the efficiency of neutrino heating
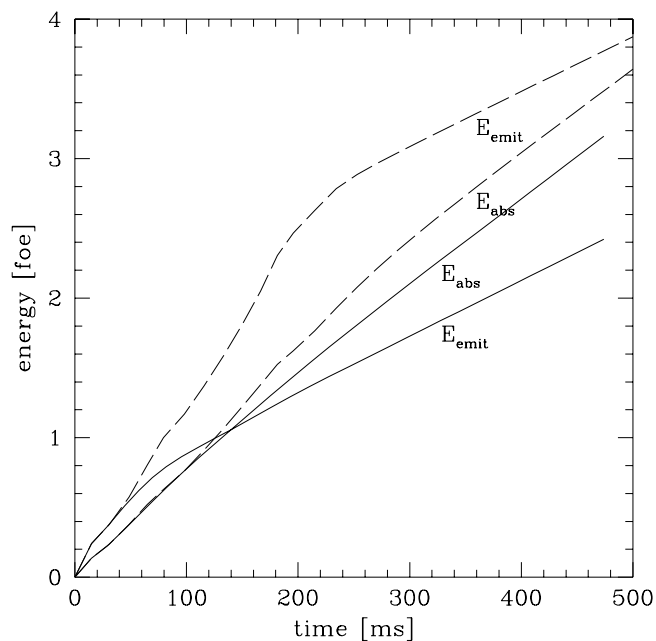

FIG. 16.—Accumulation of the absorbed and emitted energies due to neutrino heating and cooling, respectively. *Solid line:* $l_z/l_x = 1.2$ (*facg1247*); *dashed line:* $l_z/l_x = 1.0$ (spherical *facg47*). Note the difference in the emitted energy.

as discussed by Herant et al. (1994). The accumulation of absorbed energy due to neutrino heating is not so different between the anisotropic and spherical models. It is the neutrino cooling that is suppressed and contributes to the net energy gain among the neutrino interactions with matter (see Fig. 16). In other words, the suppression of the energy loss by neutrino emission is the leading factor for the explosion mechanism. This is similar to the mechanism proposed by Burrows et al. (1995). In their discussion, the shock first starts to move upward, and then neutrino cooling is suppressed as a result of the decreased temperature. The cause of the shock revival, however, is different; the locally intense neutrino heating is important in our model, while an increase in the average entropy due to convective motion is not required to help the shock wave to revive, unlike their model. A temporal variation of neutrino flux in angle has also been reported in Burrows et al. (1995). This fluctuates locally and varies with time, although the typical variation in angle is relatively large at a factor of 1.6 (3.0 at the most) and the timescale is of the order of 10 ms. On the other hand, the anisotropic neutrino radiation investigated in the present paper does not change with time or vary over angle with less amplitude in neutrino flux density. We still have to investigate the case of a time-dependent fluctuation in neutrino flux.

4.2. Neutrino Luminosity

Janka & Müller (1995, 1996) have concluded that the enhancement of neutrino luminosity was most important for driving to an energetic explosion. We also confirmed the tendency like this, comparing spherical models between $T_v = 5.0$ (*facg50*), 4.8 (*facg48*), 4.7 (*facg47*), and 4.6 MeV (*facg46*) [see $E_{exp}^{(80)}$ in Table 1]: the explosion energy increased with T_v by a large factor for the spherical cases. As for the effect of the anisotropy, it was found that the less luminous the neutrino radiation was, the more important the anisotropy was. In an energetic explosion like the 5.0 MeV models, the effect of anisotropic neutrino radiation on the explosion energy was negligible. Almost no difference was found in their explosion energy (Table 1). In the marginally explosive models of 4.7 MeV, however, an anisotropy of 10% in the neutrino flux was capable of almost the same energy evolution as an enhancement of 4% in total neutrino luminosity as shown in Figure 13 and Table 1 [$E_{exp}^{(80)}$ for *facg1247* and *facg475*]. Enhancement of the total neutrino luminosity was not always necessary to drive toward an explosion. In the models of 4.6 MeV, anisotropic neutrino radiation was even more crucial for a successful explosion as shown in Figure 15 and Table 1.

4.3. Anemic Explosions

Since we do not know at present whether the neutrino luminosity in a real supernova explosion is strong enough or not, or whether it has been reproduced correctly in past simulations, we have to wait for the answer to whether anisotropy in the neutrino radiation field is generally important or not, until the neutrino opacity and the numerical technique for the neutrino transport are improved in future calculations. The anisotropy is of great importance, at least, in the case of massive stars of 40–70 $M_\odot$ at the zero-age main sequence. This is a plausible range of the critical mass between the formation of a black hole and that of a neutron star (exactly speaking, between the failure and the success of a supernova explosion, since there

is the probability of an explosion that produces a black hole; e.g., Bethe & Brown 1995). Stagnation of the shock wave is certain to take place there because of the heavy central core. The explosion should be sensitively attained or not, depending on the degree of anisotropy in neutrino radiation.

4.4. *Comparison with "Convective" Models*

The effect of anisotropic neutrino radiation was compared with that of convection (so-called in supernova research), which was reproduced by putting various initial fluctuations into the spherical model (*facg47*). This comparison was done in order to remove ambiguity due to different input physics from other supernova studies. Merely citing other authors' results is not enough. For such models, two types of initial perturbation were considered. One is a model in which only the shocked matter behind the shock is initially perturbed in density (*frho1047* and *frho1p47*; see Table 1), while the other is a model in which all the infalling matter is perturbed in density (*fr10ff47* and *fr1pff47*). The perturbation only in density is considered here for simplicity, and its profile is given by

$$\delta\rho = \alpha\rho \sin\left(n_\theta\,\theta\right), \qquad (23)$$

where $n_\theta/4 = 5$ is the number of waves as in each panel of color-scale figures (an angle $\pi/2$ from pole to equator is shown) and α represents the amplitude of the perturbation. The amplitude was chosen as $\alpha = 10\%$ and 1% (see Table 1). An amplitude less than 1% is unfortunately inapplicable since the numerical noise, even with an artificial viscosity imposed, has been estimated to be 10^{-3} (see §§ 4.11 and B4; see also Shimizu 1995). The neutrino radiation field is spherical for the convective models.

The time evolutions of the various energies for "convective" models are shown in Figures 17 and 18. It should be noted that the scales of the time axes are different.
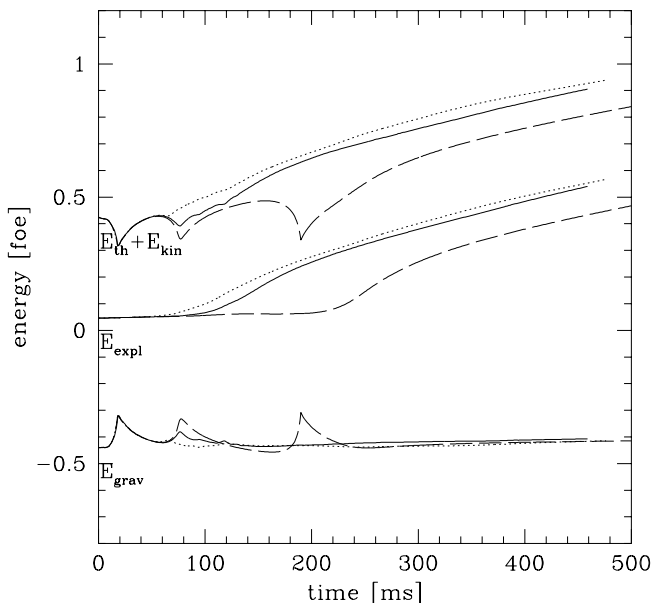

FIG. 17.—Time evolution of the energies for convective models where the initial perturbation is put only inside the shock wave. *Solid line:* $\delta\rho/\rho = 10\%$ (*frho1047*); *dashed line:* $\delta\rho/\rho = 1\%$ (*frho1p47*); *dotted line:* $l_z/l_x = 1.05$ (anisotropic but unperturbed *facg10547*). The dashed line is almost identical to that of the unperturbed spherical model (*facg47*), which is not shown here but in Fig. 18.
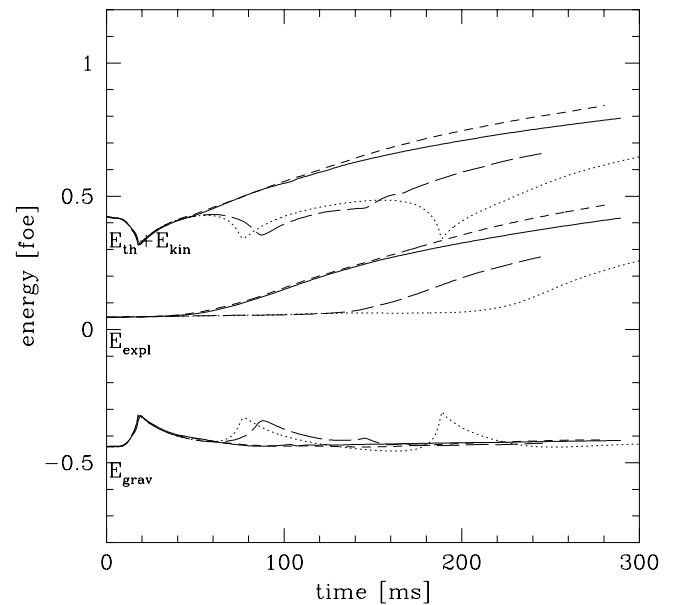

FIG. 18.—Time evolution of the energies for convective models where the initial perturbation is put all through the infalling matter. *Solid line:* $\delta\rho/\rho = 10\%$ (*fr10ff47*); *long-dashed line:* $\delta\rho/\rho = 1\%$ (*fr1pff47*); *short-dashed line:* $l_z/l_x = 1.2$ (anisotropic *facg1247*); *dotted line:* (spherical *facg47*). Note that the scale of the time axis is different from Fig. 17.

Figure 17 is for the models in which the initial density perturbation is put only inside the initial shock front (anisotropic radiation model *facg10547* is also plotted for comparison), while Figure 18 is for the models in which the initial perturbation is put all through the infalling degenerate matter (anisotropically radiative *facg1247* and spherical *facg47* are also plotted). In Figure 18, the curves for the explosion energy for anisotropic *facg1247* and perturbative *fr10ff47* show almost identical profiles [see also $E_{\mathrm{exp}}^{(200)}$ for *facg1247* and *fr10ff47* in Table 1]. An anisotropy of 10% in neutrino radiation (*facg1247*) is equivalent to a perturbation of 10% if all the infalling material is uniformly perturbed (*fr10ff47*), as far as the effect on the explosion energy is concerned. It is to be noted here that the total neutrino luminosity is kept unchanged. It is shown that the anisotropic neutrino radiation has an effect on the explosion energy comparable to the entropy-driven "convection."

The curves for the explosion energy for perturbative *frho1047* and less anisotropic *facg10547* show similar profiles in Figure 17. That is, the perturbation put only within the shock wave (*frho1047*) has a smaller effect on the explosion than the perturbation of the same amplitude ($\delta\rho/\rho = 10\%$) but put all through the infalling matter (*fr10ff47*), which shows a similar profile to more anisotropic *facg1247*. Moreover, there is a remarkable difference between model *frho1p47* (only inside the shock; $\delta\rho/\rho = 1\%$) in Figure 17 and model *fr1pff47* (all through the infalling matter; $\delta\rho/\rho = 1\%$) in Figure 18: the curves for *frho1p47* are almost identical to those for *facg47* (the spherical, unperturbed model), and the explosion energy does not increase until around 220 ms, while those for *fr1pff47* show faster energy gain from 140 ms than the spherical case; compare also $E_{\mathrm{exp}}^{(200)}$ for *frho1p47* and *fr1pff47* in Table 1. This difference is due to the fact that the matter continues to inflow through the convectively unstable region (due to neutrino heating) during the stage of the shock stalling. The crossing time of the inflowing matter is ~ 20 ms since the height of the

unstable region is 120 km between $r = 200$ and 80 km (Fig. 1e), and the velocity of inflow is $\sim 5 \times 10^8$ cm s^{-1} (Fig. 1b). The growth timescale of the convective instability is 20–50 ms, and the convective velocity is between $\sim 10^8$ cm s^{-1} in the linear growth regime and $\sim 10^9$ cm s^{-1} in the nonlinear growth regime (empirical from the simulations; see, e.g., Figs. 19 and 20); the sound velocity is also of the order of magnitude of 10^9 cm s^{-1}. Therefore, the growth time of convection and the inflow time are comparable, and these timescales are short compared with the period during the shock stalling (~ 100 ms). The perturbed matter con-

max 2.4×10⁰ min 2.2×10⁻²   3.1×10⁹ cm s⁻¹ at (300,0)

FIG. 19.—Contour map of the photon-to-baryon ratio, ϕ, and the velocity field for the perturbed model of $\delta\rho/\rho = 10\%$ and $l_z/l_x = 1.0$ (*fr10ff47*) at $t = 56$ ms after the shock stall.

max 1.8×10⁰ min 3.9×10⁻²   3.1×10⁹ cm s⁻¹ at (300,0)

FIG. 20.—Contour map of the photon-to-baryon ratio, ϕ, and the velocity field for the perturbed model of $\delta\rho/\rho = 1\%$ and $l_z/l_x = 1.0$ (*fr1pff47*) at $t = 63$ ms after the shock stall.

tinues passing through the convectively unstable region when its convective instability grows and it leaves only part of influence there. When the matter with almost no perturbation flows in the shock front, the growth of instability slows down in the locally perturbed models (*frho1047* and *frho1p47*).

The distribution of perturbation is important for the explosion mechanism in this respect. If the perturbation were to exist locally within a restricted portion of the iron core or the silicon shell, the perturbed matter would cross the convectively unstable region and soon fall onto the proto–neutron star before the convective instability could grow sufficiently and affect the explosion energy during the stalled-shock stage. The models in which the perturbation is added only behind the shock (*frho1047* and *frho1p47*) are corresponding to this case. Thus, widely distributed fluctuation is necessary for the "convective trigger (or boost)" to work sufficiently. Therefore, it should be clarified how large the perturbation is and how it is distributed in the Si and C + O shells at the onset of collapse. Bazan & Arnett (1994) have shown that perturbation of the order of 5% in density arises from convection in the oxygen-burning shell just before the onset of collapse, although its distribution is not described in detail. Both anisotropically radiating and "convective" models contribute to breaking down the spherical symmetry at the early stage of the explosion and increasing the explosion energy. Based on the present results of the numerical simulations, anisotropic neutrino radiation is established as another mechanism by which the shock wave can revive, other than the so far suggested "convective trigger."

Figures 19 and 20 show entropy contour and velocity field maps for the perturbative models of $\delta\rho/\rho = 10\%$ and 1%, respectively. It can be seen that their growth timescales of the hydrodynamical instability are largely different depending on the amplitude of the initial perturbation only. Accordingly, the increase in the explosion energy in the more perturbative model ($\delta\rho/\rho = 10\%$) is quite faster than that in the less perturbative model ($\delta\rho/\rho = 1\%$) as in Figures 17 and 18 [see also $E_{\rm exp}^{(200)}$ in Table 1]. We must be careful here because only 10% of numerical noises in collapse simulations will affect the conclusive results, which is seen in SPH simulations by Herant et al. (1994; see also § 1).

4.5. Anisotropy in Neutrino Radiation

It is possible to consider several causes for anisotropic neutrino radiation as follows. First, the convection inside the neutron star transports neutrinos outward anisotropically. Second, matter accretion on the neutron star is not spherical because of the entropy-driven convection outside. Accordingly, the accretion-originated contribution of the neutrino emission is anisotropic. Third, if the central core is a fast enough rotator, there is no reason for the system to maintain spherical symmetry. Although many models should be examined in order to investigate the effect of anisotropic neutrino radiation in detail, we consider in the next discussion (§ 4.6), as the first step, the last, simplest case of them, namely, anisotropy due to rotation.

It should be noted here that the anisotropic neutrino radiation investigated in this study has to be maintained for over 100 ms in order to increase the explosion energy sufficiently. This may be the case in which the central core is a fast enough rotator. Even without rotation, on the other hand, the neutrino flux is expected to fluctuate with angle
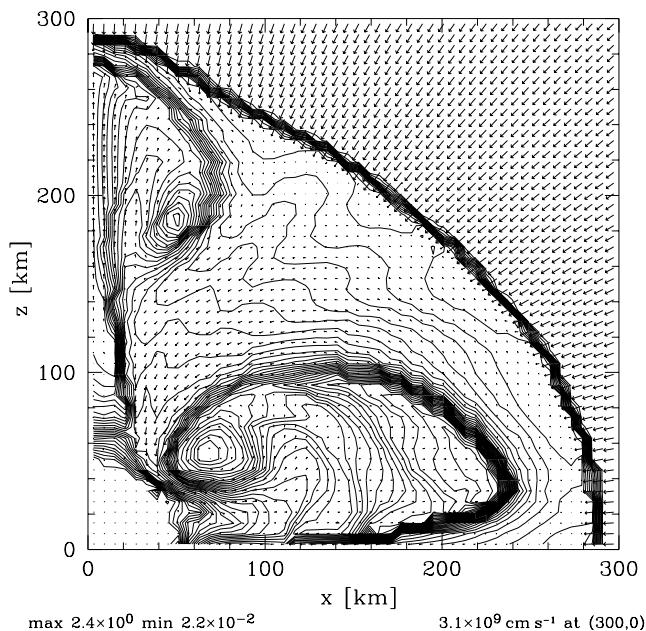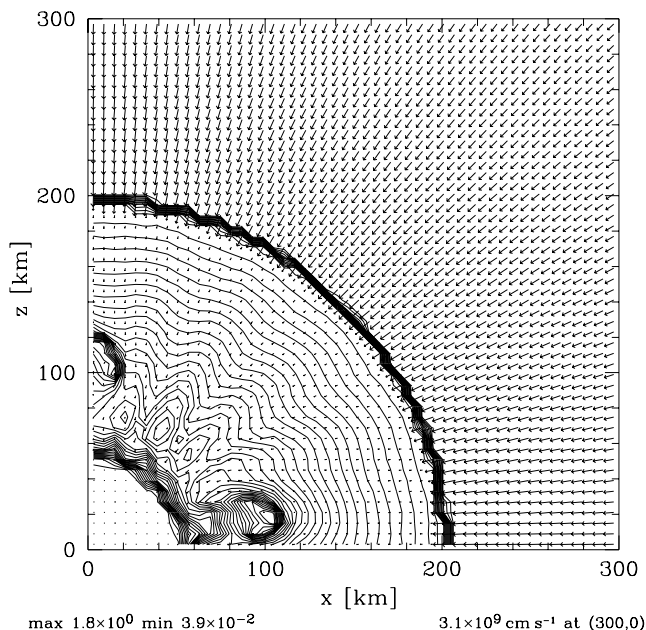
and time as a result of gravity waves around the neutrino sphere (Burrows et al. 1995). The accordingly produced hot spots will heat the surrounding gain region selectively. It would be interesting to investigate further how the gravity waves are modified if a slow rotation is put into the system. Detailed numerical simulations including these time-dependent effects are further necessary.

We only carried out the anisotropic model with the least number of modes in the angular variation of the neutrino flux (maximum at the pole and minimum at the equator) as in equation (5). A model with the higher order variation can be considered, but it would result in an almost spherical model. The neutrino luminosity at an observer is an integration of the neutrino flux over the neutrino-emitting surface that is seen from the observer (see Appendix A for details). The higher order variation of the neutrino flux on the surface is averaged and smoothed out soon; the neutrino radiation field is already almost spherical and hence the heating process. In contrast to the short-lived hot spot in the simulation by Burrows et al. (1995), a long-lived hot spot, if any, is worth taking into account, but the presented model in this paper is a good approximation to this, if the spot is placed on the axis of symmetry.

4.6. Rotation of the Central Core

Progenitors of core collapse supernovae, such as OB stars, are in general observed to be fast rotators (~ 200 km s^{-1} at the surface, $P \sim 1$ day; see, e.g., Tassoul 1978; Quirrenbach et al. 1993). Neutron stars, which are products of core collapse supernovae, are also observed as rotating pulsars (e.g., Crab pulsar: $P \sim 0.033$ s). The dimensionless angular momentum, which is defined as $q = J/(GM^2c^{-1})$, is often used for discussing stellar rotation. If $q > 1$, the rotation is so high that the centrifugal force will balance with the gravitational force during the collapse. Observation of massive progenitor stars indicates $q \sim 10$ for the central core (rigid rotation at the main-sequence phase is assumed), while that of pulsars shows at least $q \sim 10^{-3}$. Since this parameter q is conserved for an isolated system, its value for the central core at collapse is between them. The discrepancy is due to the angular momentum transport (convective or whatever) from the center to the envelope during the stellar evolution. However, the exact answer for the q value is not known.

Several researchers have considered that the rotation of the central core would not be important for the explosion energy (see, e.g., Yamada & Sato 1994; Fryer & Heger 2000). Their reasoning is that the centrifugal force would prevent a sufficient collapse of the central core and hence it would become difficult to transform large gravitational energy via neutrino radiation energy into explosion energy. This is the case in which the core is an extremely fast rotator with the q value close to unity. The situation, however, can be different as in this study if the core is rotating moderately and the anisotropic neutrino heating is taken into account. If the proto–neutron stars are rotating, centrifugal force will asymmetrically deform the neutrino emission surface on the neutron stars, and the emitted neutrinos will be focused on (or deflected from) the direction of the rotation axis. These anisotropic neutrinos then locally heat the material behind the shock wave, and, as a result, the shock wave will revive and escape from the central iron core. The rotation of the proto–neutron star itself can play an important role in the explosion phenomenon through the anisotropic neutrino

heating. Any tiny deviation from spherical symmetry in neutrino radiation will be magnified into a large explosion asymmetry, since there is a large reservoir of the gravitational energy of the neutron star that is released as neutrino radiation, the absorbed energy (a few percent) of neutrinos almost balances the emitted energy, and their small difference (about 1%) is converted into the kinetic and thermal energy of the exploding material. The effect on the explosion energy, however, is a subtle problem. It is not so easy to conclude that such a local deviation would contribute to the global explosion energy. In the present study, therefore, we carried out a systematic series of simulations to investigate the effect of anisotropic neutrino radiation on the explosion energy.

The angular velocity corresponding to each simulated anisotropic model can be estimated, for example, for the case of the Maclaurin spheroid (see Appendix A and Shapiro & Teukolsky 1983) as

$$\Omega^2 = 2\pi G\rho \left[\frac{(1-e^2)^{1/2}}{e^3} (3 - 2e^2) \arcsin e - \frac{3(1-e^2)}{e^2} \right],$$
(24)

where the eccentricity is defined by $e^2 = 1 - (a_z/a_x)^2$. The period of rotation for a given ratio of the fluxes is evaluated as follows:

$$l_z/l_x = 1.05 \leftrightarrow P = 19.4 \text{ ms} ,$$
$$l_z/l_x = 1.20 \leftrightarrow P = 10.5 \text{ ms} ,$$
$$l_z/l_x = 1.50 \leftrightarrow P = 7.7 \text{ ms} .$$
(25)

In particular, the ratio of the rotational and gravitational energy and the q value for $l_z/l_x = 1.05$ are calculated as $T/|W| = 1.3\%$ and $q = 0.63$, respectively. The angular velocity that corresponds to the assumed anisotropy in this study is not unrealistic but a little higher than that of observed isolated radio pulsars.

Moreover, the anisotropy in neutrino radiation that has been assumed in the present work is only one of the effects of rotation of the collapsed core. There are other effects of rotation that are expected to enhance an asymmetric explosion, so that the present simulations provide a demonstration of the lower limit of the effect of rotation on the supernova explosion. The other effects of rotation are considered like this:

1. In a spheroidal configuration of matter in the rotating iron core, it is easier for the shock wave and the high-entropy matter to proceed in the direction of the rotation axis where matter accretion in the outer part of the central core is less than that around the equatorial plane.

2. The temperature is distributed on the neutrino-emitting surface in which the highest value of temperature (and consequently, the highest neutrino energy) is attained on the rotation axis.

3. Aspherical convective and diffusive neutrino transfer occurs inside the rotating proto–neutron star.

The first and second effects will enhance a jetlike explosion. It has been shown (H.-T. Janka 1997, private communication; Keil 1997) that the third one gives intense neutrino flux at the pole in the very early phase of neutrino emission, but it is severely suppressed later as a result of a combined

effect of convection and rotation. However, an asymmetric explosion will result anyway, and the results strongly depend on the speed of rotation. According to the results of the present simulation, only moderate rotation is required, since the effect of anisotropy in neutrino radiation is saturated as shown in § 3. Results of explosive nucleosynthesis, moreover, prefer moderate rotation (Nagataki, Shimizu, & Sato 1998). (The circulation of the high-entropy matter at later stages of the explosion could also be affected by rotation.) These issues remain to be investigated further.

It is noted here that the symmetry axis of deformation of the exploding envelope (speckle image; Papaliolios et al. 1989; Cropper et al. 1988) at early time (several months) is not aligned with that of the ring around SN 1987A (*HST* image; Jakobsen et al. 1991); the difference in the projected angle on the sky is as large as 30°. The former might reflect the nature of the explosion, while the latter presumably indicates the rotation axis of the progenitor star at the supergiant phase. These observations can neither support nor reject the rotator model. It is only clear that the asymmetry in the speckle image is not of the rotational origin alone (either in the core or in the envelope). The asymmetry still has to be explained in another way (such as clumping of expanding envelope or a combination of various effects). We have not obtained enough information on the original asymmetry in the explosion of the supernova core yet. In the case of a close binary system, the central core of the supernova progenitor can be a fast enough rotator, since the angular momentum transport from the central core to the envelope does not work as much as that in a single star after its envelope is stripped during the Roche lobe flow. Some supernova explosions at least will have rotating cores. Moreover, there is a possibility to observe the original asymmetry in the explosion of the core since such a star often appears to be stripped of the H and He envelopes (see Wang et al. 2001).

4.7. Observed Asymmetry in Supernova Explosions

The jetlike explosion (due to rotation or whatever) seen in the simulations may be the origin of the observed asymmetry in the envelopes of SN 1987A, SN 1993J, and others (Cropper et al. 1988; Papaliolios et al. 1989; Trammell et al. 1993; Wang et al. 2001). In the case of SN 1987A, the rotational origin is rejected and another mechanism is necessary for the anisotropy of the neutrino flux if this is the case. We must be careful, however, because the initial asymmetry of the explosion in the central core tends to diminish in the course of shock propagation in mostly spherical progenitor envelopes (Chevalier & Soker 1989; Ishikawa et al. 1992). The degree of asymmetry finally observed in the explosion depends on the asymmetries in both the central core and the envelope (and even in the surrounding interstellar matter). Nevertheless, it is to be noted that the degree of initial asymmetry obtained in the present simulations is comparable to that required for SN 1987A; it has been estimated in Ishikawa et al. (1992) that two times the difference in the initial explosion energy anisotropy with the assumption of the spherical configuration of the envelope has the comparable effect to asymmetry due to the plausible rotational configuration of the hydrogen envelope. It is still possible that the axis of asymmetry deviated from the one due to the hydrogen envelope by the effect of the initial asymmetry due to anisotropic neutrino radiation. It should also be noted that there is a naked-core explosion that has been observed

to be asymmetric by Wang et al. (2001), whose detailed observation can reveal the nature of supernova explosions.

4.8. Kick Velocity

The kick velocity of a high-velocity pulsar may also be explained if jetlike convective motion occurs asymmetrically between the northern and southern hemispheres, which could be due to instability inside the neutron star or to severe sensitivity of the bubble convection to the local neutrino flux. Since the maximum velocity of convection in Figures 2 and 3 is nearly 3×10^9 cm s^{-1} and the associated mass is between 10^{-2} and 10^{-1} $M_\odot$, the estimated pulsar velocity can be in the range ~ 200–2000 km s^{-1} (the highest pulsar velocity observed is ~ 1500 km s^{-1}). In fact, we found, as a preliminary result, that a neutron star can be accelerated to the velocity of 105 km s^{-1} within 200 ms for the $l_z/l_x = 1.2$ model (*facg12*), by calculating an integral of the momentum distribution of the exploding material with an assumption of a spherical explosion over one of the hemispheres. This is similar to the result of Janka & Müller (1994).

4.9. The r-Process

As can be seen from Figures 2 and 3, it was found neither that the hot bubbles are shell-like nor that the thermodynamical variables are those averaged over solid angles of the same radius. We have to do r-process network calculations mass element by mass element. In fact, Woosley et al. (1994) have pointed out that the multidimensional effect, namely, convection acting on the r-process nucleosynthesis, is important to fit the solar abundance of r-process nuclei. If this is the case, we have to calculate the r-process nucleosynthesis coupled with the multidimensional collapse simulation.

4.10. Neutron Star Mass and Ni Production

Two problems, small baryon mass of the produced neutron star and Ni overproduction, are often reported in simulations of basically spherical models in which convective motion breaks spherical symmetry but the shock wave is mostly spherical (Herant et al. 1994; Janka & Müller 1996; Burrows et al. 1995). It seems that the enhancement of the total neutrino luminosity is favorable for the explosion energy but not for the neutron star mass or for the explosive Ni production, since a large amount of matter is blown off by an energetic shock wave. The jetlike anisotropic explosion model, however, provides a new way to solve these problems. This is because, in this model, only part of matter in the outer part of the collapsed core is exploded in the direction of the intense neutrino flux and because an additional amount of matter around the plane orthogonal to it, where the explosion is weak, falls onto the proto–neutron star as shown in Figures 2, 3, 4, and 5. (This infall could further contribute to enhancement of neutrino luminosity. This ceases at the later stage after the expansion of the shock wave; see Fig. 11.)

4.11. A Problem with Artificial Viscosity

An artificial viscosity has been input in order to suppress numerical oscillation whose amplitude can be as much as 1% in the downstream side behind the standing shock wave. Moreover, artificial viscosity that deals with two dimensions is essential in order to achieve the synchronization of the shock jump along the shock front. The defi-

nite formula of numerical artificial viscosity is presented in § B4. The effect of artificial viscosity has been investigated by varying its coefficient, K, that is defined in equation (B24).

For energetic explosion models, the effect of artificial viscosity was relatively small. It only changed the growth of instability at the top of the high-entropy bubble as seen in Figure 2 and in Figures 21a and 21b. It should be noted here that this region is strongly unstable because of the inverted and steep entropy gradient. The only differences are the artificial viscosity term (eq. [B24]) that is input at the shock front and whether a very small perturbation is provided or not there. The less artificial viscosity was input, and the larger numerical noises were generated at the shock front on the downstream side. These noises served as perturbation in the convectively very unstable region and affected the growth of the instability.

On the other hand, for marginally explosive models in which $T_\nu = 4.7$ MeV, a different amount of artificial viscosity resulted in a different asymmetry in the explosion. This can be found by comparing Figure 4 with Figures 22a and 22b. The numerical noise produced at the shock front is larger because of failure in estimating the speed of the slowly moving shock wave in the numerical scheme, since a
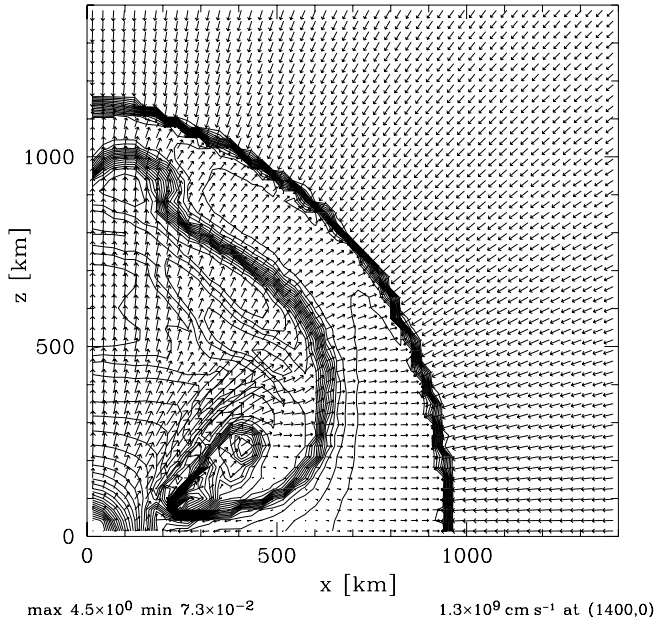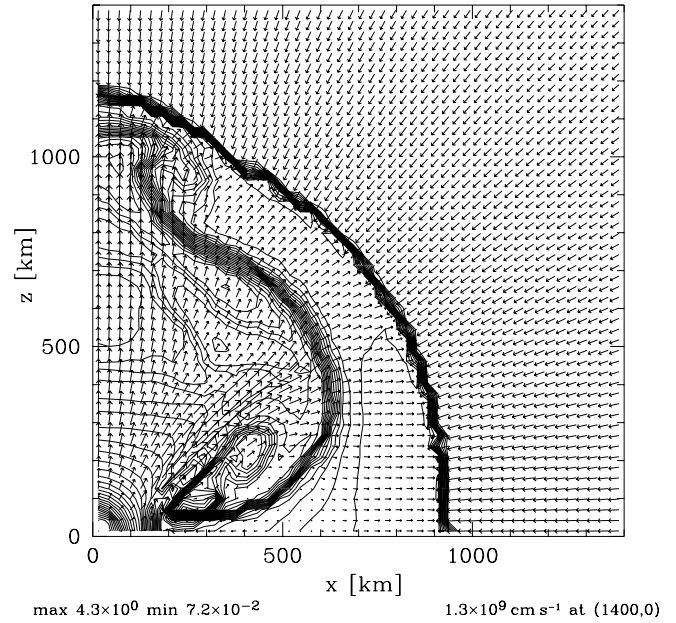

max 4.5×10^0 min 7.3×10^{-2} 1.3×10^9 cm s^{-1} at (1400,0)

Fig. 21a

max 4.3×10^0 min 7.2×10^{-2} 1.3×10^9 cm s^{-1} at (1400,0)

Fig. 21b

FIG. 21.—Same model as Fig. 2 (facg12, $K = 1.0$), except that the artificial viscosity is less input. (a) $K = 0.5$; (b) $K = 0.2$.
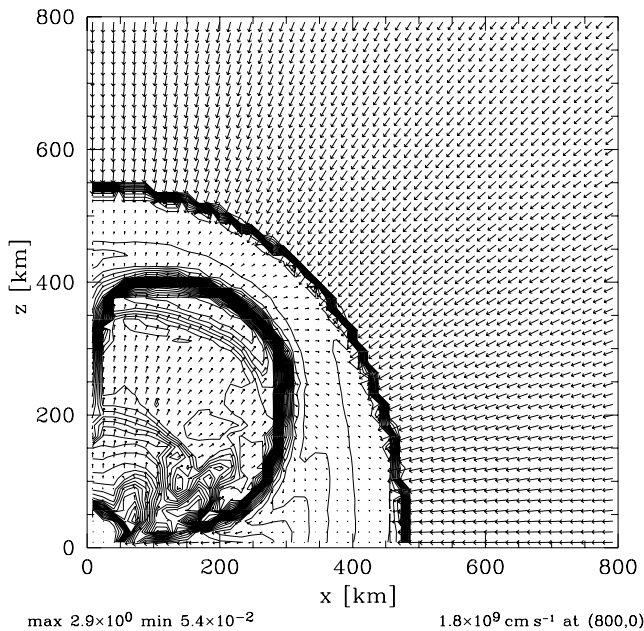

max 2.9×10^0 min 5.4×10^{-2} 1.8×10^9 cm s^{-1} at (800,0)

Fig. 22a

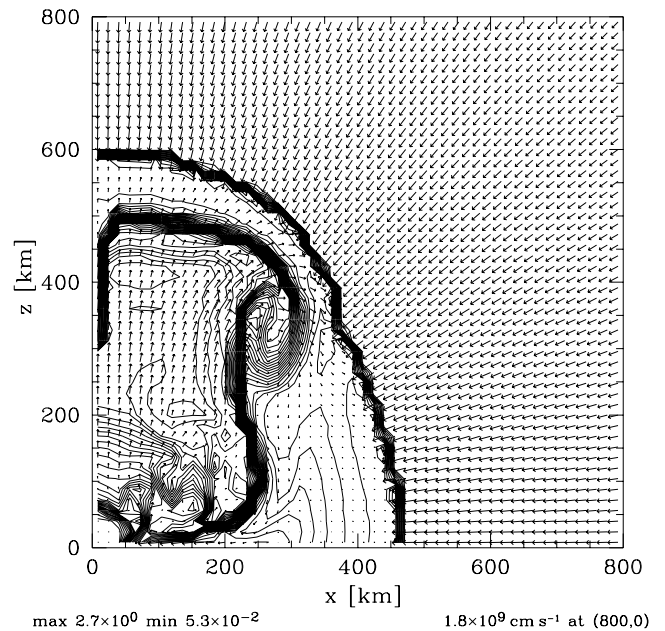max 2.7×10^0 min 5.3×10^{-2} 1.8×10^9 cm s^{-1} at (800,0)

Fig. 22b

FIG. 22.—Same model as Fig. 4 (facg1247, $K = 1.0$), except that the artificial viscosity is less input. (a) $K = 0.5$; (b) $K = 0.2$. Note the growth of instability behind the shock.

numerical spiky structure, which is an indication of such a numerical error, was observed on the shock front in a model with lower viscosity (a closer look of Fig. 22b; see also Shimizu 1995 for details). The model with artificial viscosity $K = 1.0$ is more reliable since such a spiky structure was not seen in Figure 4. The effect of artificial viscosity is yet to be investigated for further confirmation. It was found, however, that time evolutions of various energies were all the same for models even with different degrees of artificial viscosity [compare $E_{exp}^{(80)}$ of *facg1247*, *fk021247*, *fk051247*, *facg12*, *fk0212*, *fk0512*, *facg15*, and *fk0215* in Table 1]. Thus, the results for the explosion energy in the present study are not modified by the effect of artificial viscosity.

5. CONCLUSIONS

The accurate two-dimensional axisymmetric numerical simulations in the present study have revealed the effect of the anisotropic neutrino radiation on the explosion energy. It was found that locally intense neutrino emission along the axis of symmetry was adequate to revive a stalled shock wave, which leads to the explosion. This means that anisotropic neutrino radiation is capable of triggering a supernova explosion. Enhancement of the neutrino luminosity over the total solid angle is not necessarily required, although it is true that the explosion energy can be explained if the total neutrino luminosity is sufficiently high. The least required anisotropy in the neutrino flux is as

much as 2.5% in amplitude in order to affect the explosion energy. This is a plausible value for many supernova events.

It has also been shown in this study that there could be some correlation between the rotational velocity of fast-rotating neutron stars and the explosion energy of supernovae (and also the asymmetry of the explosion) owing to the effects of anisotropic neutrino radiation and local neutrino heating and cooling. The mechanism described in the present paper is effective in such a situation as in a close binary system where a relatively fast-rotating core is expected. It will also affect the critical mass between the production of neutron stars and that of black holes. These series of simulations prompt us to introduce a new idea to the supernova study, that is, " globally anisotropic neutrino radiation and locally intense neutrino heating." What is most important is that anisotropic neutrino radiation, or local neutrino heating, is suggested as a meaningful key to the explosion mechanism of supernovae.

APPENDIX A

ANISOTROPIC MODEL FOR NEUTRINO RADIATION

The background and a brief derivation of anisotropy in neutrino radiation assumed in § 2.2 are described here. The main aim of the present study was to investigate merely the effect of anisotropy, so that we adopted the simplest model of all: the neutrino sphere deformation model. We assumed the rotating configuration of the neutron star to be the Maclaurin spheroid. The surface of the Maclaurin spheroid is given by

$$\frac{x^2 + y^2}{a_x^2} + \frac{z^2}{a_z^2} = 1 \, , \tag{A1}$$

where the z-axis is the axis of symmetry and a_x and a_z ($a_x > a_z$) are the semimajor and semiminor axes of the spheroid, respectively. The surface area of the spheroid is calculated as

$$S(a_x, a_z) = 4\pi a_x^2 \frac{1}{2} \left\{ \frac{1}{(a_x/a_z)\sqrt{(a_x/a_z)^2 - 1}} \log \left[\sqrt{\left(\frac{a_x}{a_z}\right)^2 - 1} + \frac{a_x}{a_z} \right] + 1 \right\} . \tag{A2}$$

We also assumed blackbody radiation of neutrinos with a uniform neutrino temperature, T_ν, from the surface of the spheroid. The neutrino flux that is radiated from an infinitesimal surface of a blackbody to an observer is given by

$$dJ_\nu = \frac{7}{16} \frac{4\sigma}{c} T_\nu^4 \frac{d\Omega}{4\pi} dS \, c \cos \theta \, , \tag{A3}$$

where σ is the Stefan-Boltzmann constant, θ is the angle between the direction of the flux and the normal to the surface, dS is the area of the surface, and $d\Omega$ is the solid angle around the direction of the flux. The factor 7/16 is multiplied since neutrinos are Fermi-Dirac particles and have only a left-handed spin. An integration over 2π solid angles yields $dJ_\nu = (7/16)dS \, \sigma T_\nu^4$, and the total luminosity is easily obtained as $L_\nu = (7/16)S(a_x, a_z)\sigma T_\nu^4$.

The radiation flux of neutrinos at a distant observer far from the spheroid can be evaluated as follows. The ratio of the solid angle ($d\Omega/4\pi$) in equation (A3) is given by that of the area ($\pi\rho^2/4\pi r^2$), where $\pi\rho^2$ and r are the area normal to the passing flux at the observer and the distance between the observer and the spheroid, respectively. The local flux density at the observer is then defined by $l_\nu = [\int (dJ_\nu/dS)dS/\pi\rho^2]$. In order to calculate the flux density, all we have to do is to evaluate the projected area, $\int dS \cos \theta$, of the spheroid seen from the observer. A straightforward geometrical calculation yields the local flux

density as

$$l_\nu(r,\ \theta) = \frac{7}{16}\ \sigma T_\nu^4\ a_x\ \frac{\sqrt{a_x^2 \cos^2 \theta + a_z^2 \sin^2 \theta}}{r^2}\ , \tag{A4}$$

where θ is the angle between the axis of symmetry and the direction to the observer. Note that the neutrino flux in the polar and equatorial directions, l_z and l_x, is proportional to the projected area of the spheroid seen from each respective observer as follows:

$$l_z(r) \equiv l_\nu(r,\ \theta = 0°) \propto \pi a_x^2\ ,$$

$$l_x(r) \equiv l_\nu(r,\ \theta = 90°) \propto \pi a_x a_z\ , \tag{A5}$$

so that the ratio of flux is related to that of the axis as $l_z/l_x = a_x/a_z$. Note also that the total luminosity over the entire solid angle is calculated as

$$L_\nu = \int d\Omega\, r^2 l_\nu = \frac{7}{16}\ \sigma T_\nu^4 S(a_x,\ a_z)\ , \tag{A6}$$

where $S(a_x,\ a_z)$ is identical to the surface area of the spheroid (eq. [A2]).

The total luminosity has been fixed between the anisotropic and spherical models for the same neutrino temperature (§ 2.2). As a matter of fact, the scale of the axis a_x was calculated for the given ratio, $a_x/a_z = l_z/l_x$, by setting

$$S(a_x,\ a_z) = 4\pi R_{NS}^2\ , \tag{A7}$$

where $R_{NS} = 50$ km is the radius of the proto–neutron star for the spherical model.

APPENDIX B

NUMERICAL SCHEME

In the present simulations, the numerical technique has been improved from that used in the previous studies (Yamada, Shimizu, & Sato 1993; Shimizu, Yamada, & Sato 1993, 1994; Yamada & Sato 1994). An extended Roe scheme for general equations of state was applied in spherical coordinates. A generalized version of the Roe scheme has been devised (Hanawa, Nakajima, & Nobuta 1994; Shimizu 1995, 1996) that satisfies all the items of "property U" (Roe 1981) and is capable of reproducing stationary strong shock waves. Various comparative tests show us that the Roe scheme is no less accurate than the Godunov scheme, which uses the exact solution to the Riemann problem. The accuracy purely depends on the variable interpolation method, not the hydrodynamical scheme itself. The new scheme is expected to be more efficient in computational speed as well as in coding feasibility than other Godunov-type schemes like PPM, which is often used in supernova simulations.

On the other hand, a linearized Roe-like scheme was used in our previous studies (Yamada et al. 1993; Shimizu et al. 1993, 1994; Yamada & Sato 1994). The linearized scheme has the problem that the estimate of the shock speed is sometimes incorrect, especially for stalled shock waves. As for a spherical explosion model using the Roe-like scheme, this numerical error is extremely serious so that even qualitative results, especially the shock position and the energy evolution, are incorrect. However, the numerical error is only severe for spherical models in which a weak shock stalls for a relatively long time. The qualitative conclusion in Shimizu et al. (1994) is not changed since only an anisotropic model was discussed there, and the asymmetric properties in the explosion have also been reproduced in the new scheme here.

In the following part, the extended Roe scheme for general equations of state is briefly presented in §§ B1 and B2, and some cautions are advised when applying the scheme to spherical coordinates $(r,\ \theta)$ in §§ B3 and B4. For details of the used numerical scheme, see Shimizu (1995), in which the various issues on the numerical scheme, including the numerical tests, numerical errors, and comparison between schemes, are extensively discussed.

B1. ROE SCHEME FOR GENERAL EQUATIONS OF STATE AND SPHERICAL COORDINATES

In general situations, such as supernova explosions, the EOS deviates from the ideal γ-law EOS. The original Roe scheme, however, is only well defined under the condition of the ideal EOS. The Roe scheme is one of Godunov-type schemes, in which a Riemann problem is solved to estimate the fluxes on the numerical cell boundaries. Roe (1981) has proposed an approximate solution to a Riemann problem in order to reduce the heavy computational load of the Godunov scheme. He defined a matrix $\tilde{A}$ that is a function of q_R and q_L, where $q = (\rho,\ \rho u_r,\ \rho u_\theta,\ \rho E)^T$, $E = e + u^2/2$, and the subscripts "R" and "L" denote the values at the numerical cell boundary on the right- and left-hand sides, respectively. He then required a set of four conditions for this matrix $\tilde{A}(q_R,\ q_L)$:

1. It constitutes a linear mapping from the vector space q to the vector space F.
2. As $q_L \to q_L \to q$, $\tilde{A}(q_R,\ q_L) \to A(q)$, where $A = \partial F/\partial q$.
3. For any $q_R,\ q_L,\ \tilde{A}(q_R,\ q_L) \times (q_R - q_L) = F_R - F_L$.
4. The eigenvectors r_i of $\tilde{A}$ are linearly independent.

Here the flux vector is defined as $F = (\rho u_r,\ \rho u_r^2 + p,\ \rho u_\theta u_r,\ \rho H u_r)^T$ and $H = h + u^2/2$. This set of conditions is often called "property U." The flux vector F_* on the numerical cell boundary is then calculated from the eigenvalues λ_i ($i = 1,\ \ldots,\ 5$)

and the corresponding eigenvectors r_i of $\tilde{A}$ as

$$F_* = \frac{1}{2}(F_R + F_L) - \frac{1}{2}\sum_i |\lambda_i| \Delta a_i r_i \,, \tag{B1}$$

where Δa_i are defined as $\Delta F = \sum_i \lambda_i \Delta a_i r_i$. It has been shown by Shimizu (1995) that, in order to simulate the standing shock waves correctly, it is important to satisfy all the items of Roe's "property U," especially property (iii), that is, a linear relationship even under finite difference. In many cases, however, deviation from ideal gas is not so large like supernova matter. It is, therefore, preferable that the extended Roe scheme only includes correction terms from the original Roe scheme. It was the proportionality between the pressure and the internal energy of the γ-law EOS that substantially facilitated constructing an original Roe's matrix. It was found that all we have to do to construct Roe's matrix $\tilde{A}(q_R, q_L)$ for the general EOS is first to assume the following relation among the differences in the thermodynamical variables, $\Delta\rho = \rho_R - \rho_L$, $\Delta(\rho e) = (\rho e)_R - (\rho e)_L$, and $\Delta p = p_R - p_L$:

$$\Delta p = \tilde{\beta}\Delta\rho + \tilde{\alpha}\Delta(\rho e) \,, \tag{B2}$$

and then to find the coefficients, $\tilde{\alpha}$ and $\tilde{\beta}$. For the ideal EOS, note that $\tilde{\beta} = 0$ and $\tilde{\alpha} = \gamma - 1$. It is discussed later how to define those coefficients.

The assumption of equation (B2) allows us to choose the same parameter vector as in Roe (1981),

$$w = \rho^{1/2}\begin{pmatrix} 1 \\ u \\ v \\ w \\ H \end{pmatrix}. \tag{B3}$$

It is then straightforward to show that Roe's matrix $\tilde{A}$ is given by

$$\tilde{A} = \begin{pmatrix} 0 & 1 & 0 & 0 & 0 \\ -u_M^2 + \frac{\tilde{\alpha}}{2}(u_M)^2 + \tilde{\beta} & (2-\tilde{\alpha})u_M & -\tilde{\alpha}v_M & -\tilde{\alpha}w_M & \tilde{\alpha} \\ -v_M u_M & v_M & u_M & 0 & 0 \\ -w_M u_M & w_M & 0 & u_M & 0 \\ -H_M u_M + \frac{\tilde{\alpha}}{2}(u_M)^2 u_M + \tilde{\beta}u_M & H_M - \tilde{\alpha}u_M^2 & -\tilde{\alpha}v_M u_M & -\tilde{\alpha}w_M u_M & (1+\tilde{\alpha})u_M \end{pmatrix}, \tag{B4}$$

where the Roe averages are defined by

$$u_M = \frac{\sqrt{\rho_R}\,u_R + \sqrt{\rho_L}\,u_L}{\sqrt{\rho_R} + \sqrt{\rho_L}} \,,$$

$$v_M = \frac{\sqrt{\rho_R}\,v_R + \sqrt{\rho_L}\,v_L}{\sqrt{\rho_R} + \sqrt{\rho_L}} \,,$$

$$w_M = \frac{\sqrt{\rho_R}\,w_R + \sqrt{\rho_L}\,w_L}{\sqrt{\rho_R} + \sqrt{\rho_L}} \,,$$

$$H_M = \frac{\sqrt{\rho_R}\,H_R + \sqrt{\rho_L}\,H_L}{\sqrt{\rho_R} + \sqrt{\rho_L}} \,. \tag{B5}$$

Note that Roe's matrix for ideal gas is easily recovered by setting $\beta = 0$ and $\alpha = \gamma - 1$ and that Roe's property (ii) (consistency in the limit of continuity) is easily confirmed. In order to obtain the eigenvalues of the matrix, a calculation of a determinant yields

$$\det(\tilde{A} - \lambda I) = (\lambda - u_M)^3 \left\{ -(\lambda - u_M)^2 + \left[\tilde{\alpha}H_M - \frac{\tilde{\alpha}}{2}(u_M)^2 + \tilde{\beta} \right] \right\}. \tag{B6}$$

Therefore, the eigenvalues of Roe's matrix are

$$(\lambda_1, \lambda_2, \lambda_3, \lambda_4, \lambda_5) = (u_M + c, u_M, u_M - c, u_M, u_M) \,, \tag{B7}$$

where the "effective" sound velocity, c, is necessarily defined by

$$c^2 = \tilde{\alpha}\left[H_M - \frac{(u_M)^2}{2} \right] + \tilde{\beta} \,. \tag{B8}$$

The corresponding eigenvectors are

$$(r_1, r_2, r_3, r_4, r_5) = \begin{pmatrix} 1 & 1 & 1 & 0 & 0 \\ u_M + c & u_M & u_M - c & 0 & 0 \\ v_M & v_M & v_M & 1 & 0 \\ w_M & w_M & w_M & 0 & 1 \\ H_M + u_M c & \dfrac{(u_M)^2}{2} - \dfrac{\tilde{\beta}}{\tilde{\alpha}} & H_M - u_M c & v_M & w_M \end{pmatrix},$$

(B9)

respectively. It is remarkable that the newly defined variables, $\tilde{\alpha}$ and $\tilde{\beta}$, appear only in the fifth component of r_2 and in the effective sound velocity squared, c^2, and that there is no other additional term in these equations for the extended version of the Roe scheme. It is obvious that this extended scheme includes the original. The differences $\Delta q = q_R - q_L$ and $\Delta F = F_R - F_L$ between the neighboring hydrodynamical states can then be decomposed by the eigenvectors as

$$\Delta q = \sum_i \Delta a_i r_i$$

(B10)

and

$$\Delta F = \sum_i \lambda_i \Delta a_i r_i .$$

(B11)

The coefficients in these equations are given by

$$\Delta a_1 = \frac{\Delta p + \rho^* c \Delta u}{2c^2} ,$$

$$\Delta a_2 = \Delta\rho - \frac{\Delta p}{c^2} ,$$

$$\Delta a_3 = \frac{\Delta p - \rho^* c \Delta u}{2c^2} ,$$

$$\Delta a_4 = \rho^* \Delta v$$

$$\Delta a_5 = \rho^* \Delta w ,$$

(B12)

where the geometrically averaged density is defined by

$$\rho^* = \sqrt{\rho_R \rho_L} .$$

(B13)

It is to be noted here that the arithmetical average $\bar{\rho} = (\rho_R + \rho_L)/2$ is not necessary at all. It is then easy and straightforward to show that equation (B12) satisfies equation (B10) with the use of the postulated relation, equation (B2). Note that the first and third lines of equation (B12) are Riemann invariants in the limit of continuity.

The remaining problem is how to define $\tilde{\alpha}$ and $\tilde{\beta}$. Following a procedure that Roe (1981) has proposed, one can choose the coefficients for general equations of state as

$$\tilde{\alpha} = \int_0^1 \left[\frac{\partial p}{\partial(\rho e)} \right]_\rho (\theta) d\theta ,$$

$$\tilde{\beta} = \int_0^1 \left(\frac{\partial p}{\partial \rho} \right)_{\rho e} (\theta) d\theta ,$$

(B14)

where the parameter θ varies from 0 to 1 along a straight path between $(\rho, \rho e)_R^T$ and $(\rho, \rho e)_L^T$, so that

$$\begin{pmatrix} \rho \\ \rho e \end{pmatrix} (\theta) = \begin{bmatrix} \rho_L \\ (\rho e)_L \end{bmatrix} + \theta \begin{bmatrix} \Delta\rho \\ \Delta(\rho e) \end{bmatrix} .$$

(B15)

However, this method, which we call the "numerical integration" method, is heavy in computation, since we have to perform numerical integrations. Another possible method is to use equation (B2) contrarily as a definition of the coefficients $\tilde{\alpha}$ and $\tilde{\beta}$, which we call the "numerical difference" method. Only one of the two coefficients is defined with the differences, $\Delta\rho$, $\Delta\rho e$, and Δp, while the other has to be given by hand; some approximation must be introduced instead of the computational convenience in this method.

Glaister (1988) and Toumi (1992) have generalized the Roe scheme for general equations of state. In both of their schemes, however, difference $\Delta\rho$ appears explicitly in denominators, and some terms such as $\Delta p/\Delta\rho$ are replaced by derivatives like $\partial p/\partial\rho$ if $\Delta\rho = 0$. Nevertheless, the accuracy in a numerical derivative $\Delta p/\Delta\rho$ is unclear if $\Delta\rho \approx 0$ but $\Delta\rho \neq 0$.

However, it has been shown that such a difficulty is removed in the "numerical difference" method. The additional term in the fifth component of the eigenvector r_2 (eq. [B9]) is, in general, written as

$$-\frac{\tilde{\beta}}{\tilde{\alpha}} = \frac{\Delta(\rho e) - \Delta p \{[H_M - (u_M)^2/2]/c^2\}}{\Delta\rho - \Delta p/c^2} .$$

(B16)

It is amazing that the same variable appears in the denominator of equation (B16) as that in the coefficient of the eigenvector r_2: $\Delta a_2 = \Delta\rho - \Delta p/c^2$. Even if $\Delta\rho - \Delta p/c^2 = 0$, the additional term r_2 is multiplied by Δa_2 in advance as follows:

$$\Delta a_2\, r_2 = \begin{pmatrix} \Delta a_2 \\ \Delta a_2\, u_M \\ \Delta a_2\, \dfrac{(u_M)^2}{2} + \Delta(\rho e) - \Delta p\, \dfrac{H_M - (u_M)^2/2}{c^2} \end{pmatrix}. \tag{B17}$$

Owing to this procedure, no numerical differential appears in the "numerical difference" method. The only problem is that there remain some possibilities of how to define the "effective" sound speed squared c^2; this is discussed in the following section.

B2. HNN METHOD

Hanawa et al. (1994) have proposed a scheme (HNN method) in which the additional term in the eigenvector r_2 is directly evaluated by the differences in variables between two neighboring states, defining

$$-\frac{\tilde{\beta}}{\tilde{\alpha}} = \varepsilon_H \equiv \frac{\Delta(\rho e) - \Delta p/(\gamma - 1)}{\Delta\rho - \Delta p/c^2}. \tag{B18}$$

The effective sound velocity is then necessarily defined from equation (B16) by

$$c^2 = (\gamma - 1)\left(H_M - \frac{u_M^2}{2}\right), \tag{B19}$$

whereas γ is given by hand as

$$\gamma - 1 = \frac{\sqrt{\rho_R}(\partial p/\partial\rho)_{s,R} + \sqrt{\rho_L}(\partial p/\partial\rho)_{s,L}}{\sqrt{\rho_R}\, h_R + \sqrt{\rho_L}\, h_L}. \tag{B20}$$

It can be shown that $\varepsilon_H \to [\partial(\rho e)/\partial\rho]_p$ when $\Delta\rho, \Delta p \to 0$ if $\Delta\rho - \Delta p/c^2 \neq 0$ so that Roe's property (ii) is satisfied. Note that the HNN method is a special case of the "numerical difference" method in § B1, where the coefficients are given by

$$\tilde{\alpha} = \frac{\gamma - 1}{1 - [(\gamma - 1)/c^2]\varepsilon_H},$$

$$\tilde{\beta} = \frac{-(\gamma - 1)\varepsilon_H}{1 - [(\gamma - 1)/c^2]\varepsilon_H}. \tag{B21}$$

There is the unresolved problem for this method that the uniqueness of definition of γ is unclear. Its uniqueness is important since the estimate of the shock speed $u_M \pm c$ depends on this definition. This scheme, however, is the simplest of the schemes for general equations of state and is the most convenient for computation. Moreover, since the scheme is extended by adding the correction term to that for the ideal EOS, the problem will not be serious for the EOS that does not largely deviate from the ideal EOS. For this reason, we have actually adopted this method for the simulations in the present paper.

B3. CURVATURE TERMS IN SPHERICAL COORDINATES

When applying spherical coordinates, the curvature term in the equation of momentum conservation (e.g., eq. [2]) should be treated as follows:

$$-\frac{\partial}{\partial r}\, F_2 - \frac{2}{r}\, \rho u_r^2 = -\frac{\partial}{\partial r}\, F_2 - \frac{\partial}{\partial(r^3/3)}\, (r^2 \rho u_r^2) + \frac{\partial}{\partial r}\, (\rho u_r^2), \tag{B22}$$

where the second component of the flux vector $F_2 = \rho u_r^2 + p$.

In place of the left-hand side of equation (B22), the right-hand side should be calculated without any explicit curvature term. It should be noted that both sides are no longer equivalent after the operation of finite difference. Here the radial momentum flux, $\rho u_r^2 = F_1^2/\rho$, in the right-hand side is estimated by composing the density ρ and the mass flux $F_1 = \rho u_r$ (the first component of the flux vector) as

$$\rho = \frac{1}{2}\, (\rho_R + \rho_L) - \frac{1}{2}\sum_i \text{sign}\,(\lambda_i)\Delta a_i\, r_i^{(1)} \tag{B23}$$

and the first component of equation (B1), respectively. The reason for this prescription is to remove serious numerical errors around both the shock front and the free-fall region in one scheme. The first term in the right-hand side of equation (B22) ensures that Roe's flux vector F is applied properly and that no serious numerical error occurs at the shock front, while the second and third terms together serve as a good estimate of the curvature term. On the other hand, the second term of the right-hand side of equation (B22), at the same time, ensures the conservation of radial momentum in regions where the radial fluid velocity is very large. Otherwise, computation sometimes results in an underestimate of the thermal energy in a free-fall

region. The first and third terms are then a good estimate of the pressure gradient since $p = F_2 - \rho u_r^2$. The corresponding term for the θ-direction is also treated likewise.

B4. ARTIFICIAL VISCOSITY FOR TWO DIMENSIONS

Artificial viscosity should be inevitably added in order to suppress numerical noises that are produced behind the stalled shock front. Colella & Woodward (1984) have pointed out that numerical oscillation occurs in a calculation of extremely strong shocks by a Godunov-type Eulerian method as well as by a Lagrangian one. Such numerical errors up to several percent will result in overestimation of convective motion in the hydrodynamically unstable region behind the shock front. In fact, we found that the results of numerical calculations without artificial viscosity substantially differed from those with it. Reducing such numerical noises is very important since convective instability always appears behind a stalled shock wave in the delayed supernova explosions as shown in § 2.3. In two-dimensional calculations, furthermore, artificial viscosity compatible with two dimensions is important in order to ensure the synchronization of the shock jumps along the shock front. In order to suppress the numerical oscillation to a level of the order of 10^{-3}, the following procedure was implemented as in Colella & Woodward (1984). The flux vector is replaced by a new flux vector including artificial viscosity terms,

$$F^{(AV)} = F - v\Delta q \, , \tag{B24}$$

where $\Delta q = q_R - q_L$ is the difference in the fluid variable vector between two adjacent grid points and $v = K \max(-\Delta u, 0)$. Here the coefficient K represents the strength of the artificial viscosity. The velocity difference would be defined as $\Delta u = u_R - u_L$ for one-dimensional calculations. (Incidentally, the entropy problem of Roe scheme in expansion fans is fixed in a similar manner.) For artificial viscosity in two-dimensional calculations, however, Δu for the cell boundary $(i + \frac{1}{2}, j)$ is evaluated by the following divergence-like formula:

$$\Delta u = \left(\frac{\Delta u_r}{\Delta r} + \frac{\Delta u_\theta}{r\Delta\theta}\right)\Delta r$$

$$= u_{r,i+1j} - u_{r,ij} + \frac{(\Delta u_\theta/r\Delta\theta)_{i+1j}\Delta r_i + (\Delta u_\theta/r\Delta\theta)_{ij}\Delta r_{i+1}}{2} \, , \tag{B25}$$

whereas the derivatives $(\Delta u_\theta/r\Delta\theta)_{ij}$ are calculated by

$$\left(\frac{\Delta u_\theta}{r\Delta\theta}\right)_{ij} = \frac{u_{\theta,ij+1} - u_{\theta,ij-1}}{r_i[\Delta\theta_j + (\Delta\theta_{j+1} + \Delta\theta_{j-1})/2]} \, . \tag{B26}$$

The velocity difference Δu is introduced in order to detect shock discontinuities only. The value of Δu should always be negatively finite at shocks, while it should be negligible at contact discontinuities and in continuous regions. It should be noted here that we do not have to calculate the exact divergence for the spherical coordinates since the purpose of the artificial viscosity is to smooth out the numerical oscillation around the shock where numerical diffusion is insufficient without it. The difference Δu for the θ-direction is defined in a similar way.

REFERENCES

Bazan, G., & Arnett, D. 1994, ApJ, 433, L41
Bethe, H. A. 1990, Rev. Mod. Phys., 62, 801
Bethe, H. A., & Brown, G. E. 1995, ApJ, 445, L129
Bethe, H. A., & Pizzochero, P. M. 1990, ApJ, 350, L33
Bruenn, S. W., & Mezzacappa, A. 1994, ApJ, 433, L45
Bruenn, S. W., Mezzacappa, A., & Dineva, T. 1995, Phys. Rep., 256, 69
Burrows, A., & Fryxell, B. 1993, ApJ, 418, L33
Burrows, A., & Goshy, J. 1993, ApJ, 416, L75
Burrows, A., Hayes, J., & Fryxell, B. A. 1995, ApJ, 450, 830
Chevalier, R. A., & Soker, N. 1989, ApJ, 341, 611
Colella, P., & Woodward, P. R. 1984, J. Comput. Phys., 54, 174
Cropper, M., Bailey, J., McCowage, J., Cannon, R. D., Couch, W. J., Walsh, J. R., Strade, J. O., & Freeman, F. 1988, MNRAS, 231, 695
Fryer, C. L., & Heger, A. 2000, ApJ, 541, 1033
Glaister, P. 1988, J. Comput. Phys., 74, 382
Hanawa, T., Nakajima, Y., & Nobuta, K. 1994, preprint, Nagoya Univ.
Herant, M., Benz, W., & Colgate, S. 1992, ApJ, 395, 642
Herant, M., Benz, W., Hix, W. R., Fryer, C. L., & Colgate, S. A. 1994, ApJ, 435, 339
Ishikawa, S., Yamada, S., Kiguchi, M., & Sato, K. 1992, A&A, 258, 415
Itoh, N., Adachi, T., Nakagawa, M., Kohyama, Y., & Munakata, H. 1989, ApJ, 339, 354
Jakobsen, P., et al. 1991, ApJ, 369, L63
Janka, H.-T., & Müller, E. 1994, A&A, 290, 496
———. 1995, ApJ, 448, L109
———. 1996, A&A, 306, 167
Keil, W. 1997, Ph.D. thesis, TU München
Keil, W., Janka, H.-T., & Müller, E. 1996, ApJ, 473, L111
Liebendoerfer, M., Mezzacappa, A., Thielemann, F.-T., Messer, O. E. B., Hix, W. R., & Bruenn, S. W. 2000 (astro-ph/0006418)

Mayle, R. W. 1985, Ph.D. thesis, Lawrence Livermore Laboratory
Miller, D., Wilson, J. R., & Mayle, R. 1993, ApJ, 415, 278
Nagataki, S., Shimizu, T. M., & Sato, K. 1998, ApJ, 495, 413
Papaliolios, C., Karovska, M., Koechlin, L., Nisenson, P., Standley, C., & Heathcote, S. 1989, Nature, 338, 565
Quirrenbach, A., Hummel, C. A., Buscher, D. F., Armstrong, J. T., Mozur-kewich, D., & Elias, N. M., II 1993, ApJ, 416, L25
Roe, P. L. 1981, J. Comput. Phys., 43, 357
Shapiro, S. L., & Teukolsky, S. A. 1983, Black Holes, White Dwarfs, and Neutron Stars (New York: Wiley)
Shigeyama, T., Nomoto, K., & Hashimoto, M. 1988, A&A, 196, 141
Shimizu, T. M. 1995, Ph.D. thesis, Univ. Tokyo
———. 1996, RIKEN Rev., 14, 27
Shimizu, T., Yamada, S., & Sato, K. 1993, PASJ, 45, L53
———. 1994, ApJ, 432, L119
Takahashi, K., El Eid, M. F., & Hillebrandt, W. 1978, A&A, 67, 185
Tassoul, J.-L. 1978, Theory of Rotating Stars (Princeton: Princeton Univ. Press)
Toumi, I. 1992, J. Comput. Phys., 102, 360
Trammell, S. R., Hines, D. C., & Wheeler, J. C. 1993, ApJ, 414, L21
Tubbs, D. L., & Schramm, D. N. 1975, ApJ, 201, 467
Wang, L., Howell, D. A., Hoeflich, P., & Wheeler, J. C. 2001, ApJ, 550, 1030
Wilson, J. R., & Mayle, R. 1988, Phys. Rep., 163, 63
———. 1993, Phys. Rep., 227, 97
Woosley, S. E., Wilson, J. R., Mathews, G. J., Hoffman, R. D., & Meyer, B. S. 1994, ApJ, 433, 229
Yamada, S., & Sato, K. 1994, ApJ, 434, 268
Yamada, S., Shimizu, T., & Sato, K. 1993, Prog. Theor. Phys., 89, 1175